

In Situ Nanotransformable Hydrogel for Chemo-Photothermal Therapy of Localized Tumors and Targeted Therapy of Highly Metastatic Tumors

Syed Baseeruddin Alvi,[#] Rajalakshmi P S,[#] Nazia Begum, Anil Bankati Jogdand, Bantal Veeresh, and Aravind Kumar Rengan*

Cite This: *ACS Appl. Mater. Interfaces* 2021, 13, 55862–55878

Read Online

ACCESS |

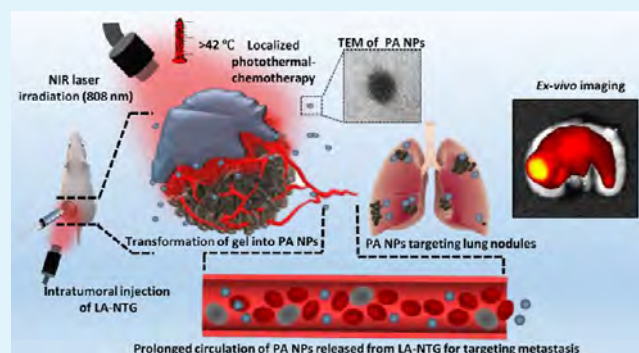
Metrics & More

Article Recommendations

Supporting Information

ABSTRACT: Metastasis is one of the predisposing factors for cancer-related mortalities worldwide. Patients with advanced cancers (stage IV) receive palliative care with minimal possibility of achieving complete remission. Antibody-based therapeutic modalities are capable of targeting tumors that are confined to a particular location but are ineffective in targeting distant secondary tumors. In the current study, we have developed a smart nanotransforming hydrogel (NTG) that transforms *in situ* to polymeric nanoparticles (PA NPs) of 100–150 nm when injected subcutaneously. These nanoparticles targeted the primary and secondary metastatic tumors for up to ~5 and ~3 days, respectively. The *in situ*-formed PA NPs also demonstrated a pH-responsive drug release resulting in about ~80% release within 100 h at 5.8 pH. When tested *in vivo*, substantial inhibition of lung metastases was observed compared to chemotherapy, thus demonstrating the efficiency of nanotransforming hydrogels in targeting and inhibiting primary and secondary metastatic tumors.

KEYWORDS: hydrogel, nanoparticles, passive targeting, melanoma, metastasis



1. INTRODUCTION

Cancer metastasis is the leading cause of death worldwide. It is estimated that the five-year survival rate of patients suffering from metastatic cancer is about 15–22%.¹ The current clinical treatment of metastasis is by systemic chemotherapy. These are administered as palliative care to alleviate the comorbidities associated with metastasis. Surgery and radiation therapy are rarely offered as treatment modalities in end-stage cancer because malignant lesions affect multiple internal organs.² Even when diagnosed at an early stage, many cancer patients often experience recurrence despite initial treatment.³ An ideal cancer treatment strategy should effectively treat both localized tumors and inhibit distant metastasis.

Near infra-red (NIR) light-based therapies like photothermal therapy (PTT) and photodynamic therapy (PDT) are the emerging cancer treatment modalities that have been extensively researched in the recent years.^{4,5} Due to its short tissue penetration depth, NIR light employed in PTT/PDT can effectively treat only localized tumors.⁶ Literature reports suggest that PTT/PDT stand-alone may not be sufficient for the complete remission of cancer. Instead, they may impart thermal/chemo-resistance to cancer cells, especially when exposed to subtherapeutic doses.⁷ The metallic, lipid, or protein nanomaterials can efficiently target primary tumors, but their

ability to target secondary/metastasized tumors is limited.⁸ This is mainly due to their short residence time and rapid clearance from systemic circulation.^{9,10} It is reported that the longer circulation time of nanoparticles is one of the major factors for efficient tumor targeting.¹¹ Thus, fabricating nanoparticles that exhibit prolonged systemic circulation time could effectively target both primary and secondary metastatic tumors. Di/Triblock copolymer based hydrogels are known to form polymeric micelles upon dissolution.¹² These micelles contain a polyethylene glycol chain on the exterior, which helps provide steric stability and prolong circulation time.¹³ The transformation of hydrogels into micelles has been reported earlier; however, investigation on their metastatic tumor targeting is warranted.^{14,15}

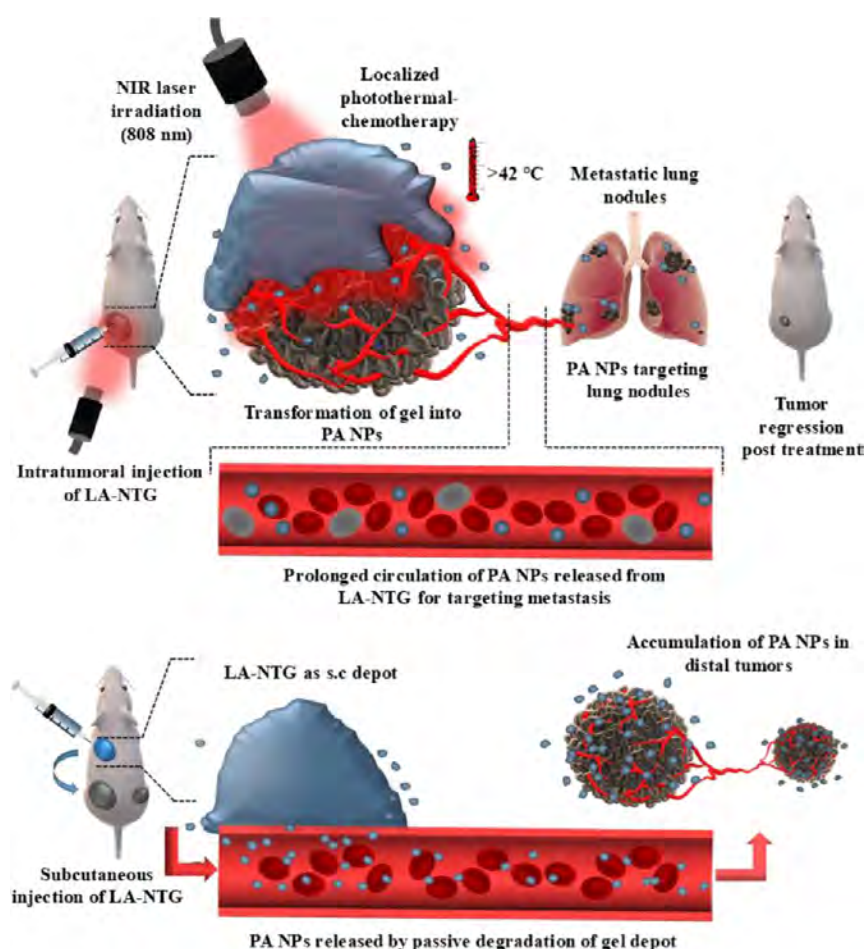
In the current study, we have fabricated an injectable nanotransforming hydrogel carrier as a multimodal therapeutic agent to treat localized tumors and inhibit metastases (Scheme

Received: September 4, 2021

Accepted: November 8, 2021

Published: November 17, 2021



Scheme 1. *In Vivo*-Localized Chemo-PTT by LA-NTG and the Inhibition of Metastatic Foci by PA NPs^a

^aThe passive degradation of the subcutaneously administered LA-NTG depot into PA NPs targeting multiple distant tumors by EPR.

1). Chemo-PTT is being rigorously studied because of its ability to inhibit localized tumors. However, literature reports on the smart hydrogel-mediated targeting of secondary tumors and adjuvant chemo-PTT are limited. In our study, we have demonstrated the ability of smart hydrogels to cause localized chemo-PTT and, in addition to it, the targeting of distant/metastasized tumors by *in situ*-formed polymeric nanoparticles (PA NPs). It is well known that following the surgical resection of the primary tumor; many patients report locoregional recurrence and distant metastasis. Those individuals treated for recurrent locoregional tumors also showed higher probability of disease recurrence at distant sites than locally.¹⁶ Currently, there are no curative therapies for metastatic relapse of cancers.¹⁷ It is worth mentioning that stand-alone chemotherapy for primary tumors exerts a paradoxical effect, which at first causes reduction in tumor size but tends to promote resistant and disseminating cancer cells.¹⁷ Taken together, the localized chemo-PTT and the tumor-targeting of smart hydrogels can be employed for treating primary and secondary tumors.

Furthermore, the literature reports on photothermally active hydrogels are based on either NIR responsive dyes or metallic nanoparticles. The hydrogel system based on NIR dyes may show high toxicity due to the leaching of the dye into the surrounding normal tissues.¹⁸ On the other hand, metallic nanosystems exhibit enhanced photothermal effects but lack degradability. We have employed a hybrid gold nanoparticle

(LA NP) as a photothermal agent in the current study owing to its photothermal stability and NIR light-mediated degradation. Due to the entrapment of LA NPs within the matrix of the smart hydrogel, repeated photothermal treatment can be performed along with the degradation of LA NPs into smaller gold nanoparticles.¹⁹ The *in situ* degradation of gold can be of significant importance as these smaller NPs can exhibit renal clearance.²⁰ Thus, the smart hydrogel presented in the manuscript holds significant potential in treating localized and metastasized tumors, demonstrating the potential for clinical translation.

2. MATERIALS AND METHODS

2.1. Materials. Pluronic F127 (PF), polyvinyl alcohol (PVA), propidium iodide (PI), fluorescein diacetate (FDA), hydrogen tetrachloroaurate(III) hydrate ($\text{HAuCl}_4 \cdot 3\text{H}_2\text{O}$), IR 780 iodide, ascorbic acid, and Doxorubicin Hydrochloride (Dox) were procured from Sigma Aldrich, and 3-(4,5-dimethylthiazol-2-yl)-2,5 diphenyltetrazolium bromide (MTT), bovine serum albumin (BSA), chloroform, and methanol were procured from SRL. Phosphate buffer saline (pH 7.4), trypsin-EDTA, DMEM, RPMI, and antibiotics [100 U/mL penicillin/streptomycin and fetal bovine serum (FBS) (US origin)] were purchased from Himedia Laboratories Private Limited (Mumbai, India). Hydrogenated soy phosphatidyl choline (HSPC) was obtained from Lipoid, Germany, as a gift sample. Deionized water (18 M Ω) was obtained from a Milli-Q synthesis system (Millipore, Billerica, MA).

2.2. Cell Lines and Maintenance. Melanoma cell lines (B16F10) and Mouse Embryonic fibroblast (NIH3T3) were procured from

NCCS Pune, India. The mouse breast cancer cell line (4T1) was procured from AddexBio (C0006004), San Diego. The melanoma cell line (B16F10) and mouse embryonic fibroblast (NIH3T3) cell line were cultured and maintained in DMEM medium, and mouse breast cancer cell lines (4T1) were cultured and maintained in RPMI medium supplemented with 10% (v/v) FBS, 1% L-glutamine, and 100 U/mL penicillin/streptomycin under standard conditions (at 37 °C in a humidified atmosphere containing 5% CO₂).

2.3. Synthesis of Liposome and Gold-Coated Liposome (LA NPs). Liposome and gold-coated liposome (LA NPs) were prepared as per published reports.²¹ Briefly, hydrogenated soy phosphatidyl choline [HSPC (Lipoid, Germany)] was used for the preparation of liposomes by the thin-film hydration method. The dried lipid film was hydrated using Milli-Q, and 2 mg/mL was kept as the working concentration. For the preparation of LA NPs, liposomes and HAuCl₄ (1:1 v/v) were mixed, and ascorbic acid was used as a reducing agent in 1:4 proportion. The reduction of HAuCl₄ by ascorbic acid on the liposome template was indicated by an immediate color change.

2.4. Synthesis of Dox Entrapping Gold-Coated Liposomes (DLA NPs). Dox was encapsulated in the liposome by the ammonium sulfate gradient method with slight modifications.²² Briefly, hydrogenated soy phosphatidyl choline (HSPC (Lipoid, Germany)) was used to prepare liposomes by the thin-film hydration method. The dried lipid film was hydrated using 240 mM ammonium sulfate at 60 °C for 1 h. The excess ammonium sulfate was replaced with PBS through centrifugation at 15,000 rpm for 30 min. The drug was added to the solution with a 20:1 lipid: drug ratio. The drug's entrapment efficiency was measured using a fluorescent spectrophotometer (RF 6000, Shimadzu, Japan). The fluorescence intensity of Dox before removing the untrapped drug (I_{total}) and the fluorescence intensity of Dox within the liposome (I_{liposome}) was measured, and the entrapment efficiency (EE %) was calculated using the formula

$$\text{EE (\%)} = I_{\text{liposome}}/I_{\text{total}} \times 100\%$$

2.5. Preparation of Thermosensitive Hydrogels (NTG and LA-NTG). The thermosensitive hydrogel was prepared by blending Pluronic F-127, PVA, and albumin. Briefly, to prepare nanotransforming hydrogels (NTGs) (without Alb), 0.6 mL of PVA solution was added dropwise to 25% ice-cold solution of Pluronic F-127 (w/w) at 4 °C under constant stirring.²³ For the preparation of NTGs (with Alb), 0.3 mL of ice-cold bovine albumin was added dropwise to this mixture under continuous stirring for 60 min. The final percentage of PVA and albumin was kept at 2 and 1.5% in 3 mL of gel solution, respectively.²⁴ For the preparation of NIR responsive hydrogel, LA NPs (400 µg/mL) were added to the above mixture and stirred at 4 °C to form LA-NTG.

2.6. Preparation of Dox Entrapping Thermosensitive Hydrogels (DLA-NTG/LA-NTG II). The LA-NTG hydrogel was added with 50 µg/300 mL Dox, which was then stirred for 15 min at 4 °C to form DLA-NTG.

2.7. Characterization of NTG and LA-NTG. **2.7.1. Thermoreversible/Irreversible Cross-Linking of NTG.** The thermoreversible/irreversible nature of the NTG (without Alb) and NTG (with Alb) was evaluated by the test tube-inversion method.²⁵ Briefly, the ice-cold mixture of the NTG (without Alb) and NTG (with Alb) solutions was injected into a glass vial and incubated first at physiological temperature (37 °C) for 10 min. Following the incubation, the glass vials were inclined to observe the fluidity of hydrogel samples. The cross-linked NTG (without Alb) and NTG (with Alb) were then incubated at 4 °C for 10 min to check the reversibility of the samples. To further evaluate the irreversible cross-linking of hydrogels, the samples were incubated for 10 min at elevated temperatures (~60 °C), and then, again at 4 °C, the glass vials were inclined to observe irreversible cross-linking.

2.7.2. Injectability and NIR Laser-Mediated Cross-Linking of LA-NTG. The prepared LA-NTG was injected through a 26 gauge syringe to evaluate the injectability into a 2 mL Eppendorf tube.²⁶ To evaluate the NIR laser mediated photothermal cross-linking of LA-NTG, the mixture was subjected to NIR laser irradiation 808 nm (650 mW, Shanghai Inter-Diff Optoelectronics Technology Ltd, Shanghai, China) for 10 min. The temperature increment was monitored using a thermal imaging camera. To determine irreversible cross-linking, LA-NTG was

incubated at 4 °C for 10 min and was inclined to check the reversibility of the samples.²⁷

2.7.3. Scanning Electron Microscopy and FTIR Analysis. The morphological analysis of NTGs at physiological temperature (37 °C) and elevated temperature (60 °C) was evaluated using scanning electron microscopy (SEM).²⁸ The samples were dropped on a clean silica wafer and then subjected to 37 and 60 °C for a duration of 10 min, respectively. In another instance, the LA-NTG samples were irradiated with NIR laser (808 nm (650 mW, Shanghai Inter-Diff Optoelectronics Technology Ltd, Shanghai, China)) for 10 min. Following the NIR laser exposure, the samples were then lyophilized and sputter-coated with gold for imaging. FTIR spectroscopy was performed on lyophilized Alb, NTG (without Alb), and NTG (with Alb), and the corresponding peaks were analyzed.

2.7.4. Rheological Characterization. A temperature-controlled rheometer (Anton Paar GmbH, Physica MCR 301) was used to evaluate the rheological properties of the LA-NTG (without Alb), and LA-NTG (with Alb) under dynamic shear conditions at a frequency of 1 Hz.²⁹ Briefly, a plate was lowered to face the specimen holder containing the hydrogel sample with ~1 mm nominal gap conducted within a temperature range of 4–37 °C with a ramp rate of 5 °C min⁻¹. Later, to evaluate the effect of thermal cross-linking of gel on viscosity, the temperature-sweep dynamic shear test was done from 60 to 4 °C.

2.8. In Vitro Drug Release. *In vitro*, NIR laser-triggered sustained release of Dox, D-NTG, and DLA-NTG was evaluated using fluorescence spectroscopy.³⁰ Briefly, 300 µL of each hydrogel containing Dox (500 µg/mL) was added to the inset (pore size = 3 µm) of the *trans*-well plate and was subjected to 808 nm laser irradiation for 10 min. These insets were then placed to the transwell containing 1 mL of PBS. The plates were incubated at 37 °C at 50 rpm. A small aliquot of PBS from the well was drawn to estimate Dox release by using fluorescence spectroscopy and replaced with fresh PBS. The concentration of Dox in each intervals was estimated using the standard curve, and cumulative release was plotted.

2.9. Drug Release from PA NPs at Different pH. **2.9.1. Extraction of the PA NPs from the LA-NTG.** The LA-NTG mixture containing Dox was incubated for cross-linking at 60 °C for 10 min. After 10 min, the gel was dissolved in PBS and centrifuged at 15,000 rpm for 20 min. The pellet was collected for calculating the entrapment efficiency and the pH-triggered release of the drug. The entrapment efficiency of the drug was measured using fluorescent spectroscopy. The entrapment efficiency (EE %) was calculated using the above mentioned method.

The release of the Dox from PA NPs was evaluated in three different pH; physiological pH (7.4), pH of the tumor microenvironment (6.4), and (5.8) in acetate buffer.³¹ Briefly, PA NPs were suspended in 1 mL of buffer with three different pH and were incubated at 37 °C at 50 rpm. The buffer from the 2 mL tube was drawn at specific time intervals to estimate the Dox released and was replenished with fresh buffer. The cumulative release of Dox was recorded, and the experiments were conducted in triplicates.

2.10. In Vitro Photothermal Efficacy of LA NPs and LA-NTG (with/without Alb). The sustained photothermal efficacy of LA NPs and LA-NTG (with/without Alb) was evaluated by using NIR laser 808 nm (650 mW) in a *trans*-well plate.³² Briefly, 300 µL of each hydrogel was added to the inset (pore size = 3 µm) of the *trans*-well plate and was subjected to 808 nm laser irradiation for 10 min. These inset wells were then placed in the well plates containing 1 mL of PBS. The sustained photothermal efficacy of LA NPs and LA-NTG (with/without Alb) was evaluated by recording the temperature at predetermined time intervals for 15 days, following NIR laser irradiation for 5 min. Subsequently, the thermal images were captured using a thermal camera (Flir, Chauvin Arnoux, CA, 1950 IR camera, USA). A small aliquot of PBS from the well was replenished with fresh PBS at each point.

2.11. Characterization of the Nanoparticles Extracted from LA-NTG. **2.11.1. Transmission Electron Microscopy.** Transmission electron microscopy (TEM, JEM-2100F, JEOL Inc, USA) imaging was performed on nanoparticles released from LA-NTG (with/without NIR light irradiation). TEM was performed by drop-casting the suspension on a copper grid.³³

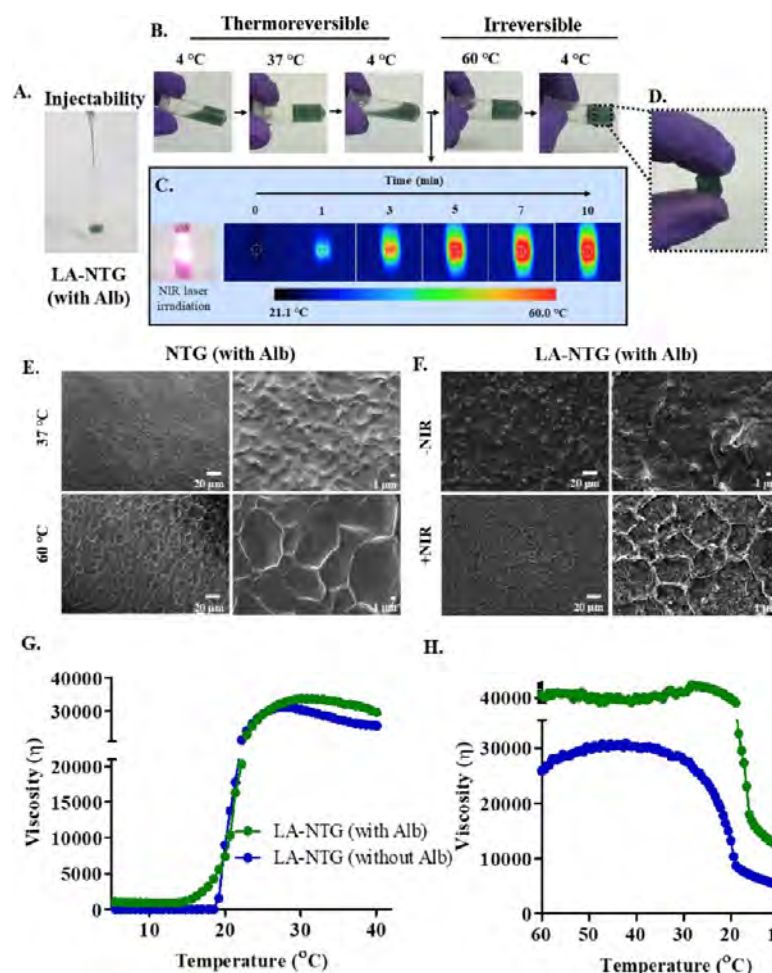


Figure 1. (A) Injectability of LA-NTG (with Alb) through a 26 gauge syringe. (B) Sol–gel and gel–sol transition of LA-NTG at 4, 37, and 60 °C. (C) Photothermal transduction of LA-NTG when irradiated with NIR light (808 nm) for 10 min. (D) Depot formation of LA-NTG post NIR light irradiation. (E) SEM images of NTG (with Alb) cross-linked at 37 and 60 °C. (F) SEM imaging showing the photothermal crosslinking of LA-NTG (with Alb) before and after NIR light irradiation. (G) Rheological studies of LA-NTG (with/without Alb) by the thermal sweep test. (H) Rheological studies showing the reverse thermal sweep test of the same sample.

2.12. In Vitro Analysis. **2.12.1. Biocompatibility of the LA-NTG Hydrogel.** The biocompatibility was evaluated in a transwell plate of pore size 3 μm using methyl thiazolyl diphenyl tetrazolium bromide (MTT) assays.³⁴ Briefly, 1×10^4 cells of normal mouse fibroblast (NIH3T3) was plated in the lower compartment of the transwell plate and incubated for 24 h. The inset containing the cross-linked hydrogel was placed in the *trans*-well plate and incubated for 24 h. MTT assay was performed in triplicates to evaluate the biocompatibility of the hydrogel.

2.12.2. Intracellular Uptake of LA-NTG I (LA NPs) and LA-NTG II (PA NPs) in a 3D Spheroid Model. The uptake of the particles released from the LA-NTG I (Dox-loaded in LA NPs) and LA-NTG II (Dox-loaded in PA NPs) hydrogels was evaluated in a 3D spheroid model of melanoma cells (B16F10) using flow cytometry and confocal microscopy. Briefly, 4×10^3 cells/drop were counted using a hemocytometer and seeded to 96 well plates coated with 1.2% agarose. After the third day, the B16F10 spheroids were transferred to the lower compartment of the transwell plate. Free Dox, LA-NTG I, and LA-NTG II were added to the upper compartment and incubated for 5 and 12 h. After the incubation, the penetration of the particles released from LA-NTG I and LA-NTG II was evaluated using confocal microscopy. Flow cytometric analysis was performed to quantify the spheroidal uptake. Dox gel control, LA-NTG I, and LA-NTG II were added to the upper compartment and incubated for 5 h with the spheroids in the lower chamber. After the incubation, the uptake was quantified using flow cytometry, and the experiment was done in triplicates.

2.12.3. Mode of Cell Death (Annexin V FITC and Propidium Iodide). The mode of cell death induced by Dox gel control, LA-NTG I, and LA-NTG II hydrogels was evaluated by flow cytometry in melanoma cells (B16F10) using annexin V FITC and propidium iodide fluorescent probes. Briefly, 5×10^3 cells were seeded in the lower compartment of the transwell plate and incubated for 24 h. 300 μL of each hydrogel was added to the inset (pore size = 3 μm) of the *trans*-well plate and incubated at 37 °C for 5 min. The inset containing the cross-linked hydrogel was placed in the *trans*-well plate and irradiated with laser for 7 min. After incubation, the cells were trypsinized and incubated with annexin V FITC and propidium iodide in a binding buffer. Later, the cells were subjected to flow cytometry.

2.13. In Vivo Experiments. The *in vivo* experiments were conducted in compliance with CPCSEA guidelines, and the Institutional Animal Ethics Committee of G. Pulla Reddy College of Pharmacy, Hyderabad, approved the protocol for conducting the study (GPRCP/IAEC/23/19/02/PCL/AE-12). Albino, Balb/C, and C57BL/6 mice were procured from Hylasco, Hyderabad.

2.13.1. In Vivo Thermal Imaging and Sustained Photothermal Transduction Efficacy. The photothermal transduction efficacy for LA NPs and LA-NTG (with/without Alb) was evaluated in albino mice (5–6 weeks old). The mice were weighed and randomly grouped into three groups (LA NPs and LA-NTG(with/without Alb)). 300 μL of samples was injected subcutaneously and irradiated with NIR light 808 nm (650 mW). The sustained photothermal transduction efficacy was measured using a thermal camera by irradiating the injected area with

NIR light in subsequent days. The temperature was recorded, and the thermal images were captured.

2.13.2. In Vivo Synergistic Chemo-PTT. The melanoma tumor-bearing mouse was established by subcutaneously injecting 1×10^6 B16F10 cells into the dorsal flank region of the C57BL/6 female mice with an average weight of about ~ 20 g. After tumor induction, when the tumor size reached an average size of 200 mm^3 , the mice were randomly divided into five groups ($n = 5$): disease control, NTG, D-NTG, LA-NTG, and DLA-NTG; $300 \mu\text{L}$ of the hydrogel was injected to the tumor, following which the injected site was irradiated with NIR 808 nm light. The NIR light irradiation lasted for 5 min, and the treatment was performed on alternative days (three treatments). The tumor sizes and body weights were measured at planned time intervals. The length, width, and height of the tumors were measured using a vernier caliper.³⁶ The organs were isolated and Hematoxylin & Eosin (H&E) staining was performed for histopathological analysis.

2.13.3. In Vivo Primary, Secondary, and Metastatic Tumor Targeting.
2.13.3.1. Sample Preparation. Hydrophobic NIR dye IR 780 was used for real-time tracking of nanoparticles. In order to track LA NPs embedded in the LA-NTG matrix, the dye was encapsulated within the liposomes and coated with gold (LA NPs); this group was termed as "LA-NTG I", whereas to track PA NPs released from LA-NTG, the dye was entrapped in a gel matrix, and the group was termed as "LA-NTG II". The dose of IR 780 was $50 \mu\text{g/mL}$ in both the gel formulations (Ex: 780 nm Em: 808 nm).

The ability of LA-NTG to target single, distant tumors, and lung metastasis was evaluated by using the small animal NIR fluorescence imaging system (IVIS Perkin Elmer). An orthotopic 4T1 tumor was established in BalB/C mice by injecting 1×10^6 cells in mammary fat pads for evaluation of single tumor targeting efficacy. $300 \mu\text{L}$ of LA-NTG I and II was injected into the animal's right upper flank. Following the injection, animals were monitored for distribution by an *in vivo* fluorescence imaging system. For evaluating the distant tumor targeting efficacy, an orthotopic 4T1 tumor was established in BalB/C mice by injecting 1×10^6 cells in mammary fat pads (both sides). One side of the tumors was injected by a delay of 3 days, following the first tumor induction ($n = 3$). $300 \mu\text{L}$ of LA-NTG I and II was injected into the animal's right upper flank. Following the injection, animals were monitored for distribution using an *in vivo* fluorescence imaging system.

The lung metastasis model was established by injecting 2×10^5 cells by i.v. route. Following the injection, animals were injected with LA-NTG I and II on the 20th day.³⁵ Later, animals were monitored for the localization of released nanoparticles ($n = 3$).

2.13.4. In Vivo Antimetastatic Evaluation.
2.13.4.1. Sample Preparation. Dox was used as a model drug for the study. In order to evaluate the antimetastatic efficacy of LA-NTG I and LA-NTG II. The spontaneous melanoma metastatic lung nodule-bearing mouse was established by intravenous injection of 2×10^5 B16F10 cells into the tail region of the C57BL/6 female mice with an average weight of ~ 20 g.³⁵ On the 10th day of tumor induction, the mice were randomly divided into four groups ($n = 5$): disease control, free Dox, LA-NTG I, and LA-NTG II. $300 \mu\text{L}$ of the hydrogel was administered subcutaneously on every 4th day, and five doses of treatment were given. After 35 days, the mice were sacrificed for the analysis of spontaneous melanoma metastatic lung nodules. The weight of the lungs was measured and compared with the normal lungs. *Ex vivo* quantification of melanin from isolated lungs of each group was also performed.³⁷ Briefly, 100 mg of the lung samples from each group was dissolved in 1 M NaOH containing 10% DMSO. The samples were heated at 80°C for 1 h and centrifuged at 3000 g for 10 min. The UV–Vis absorbance of the supernatant was measured at 410 nm.

2.14. Statistical Analysis. One-way ANOVA followed by Post-Hoc Tukey's test and unpaired *t*-test ($*P < 0.05$, $**P < 0.01$, $***P < 0.001$) was performed to compare the different groups.

3. RESULTS AND DISCUSSION

Chemo-PTT has shown promise in treating localized tumors due to the synergistic effect of chemotherapeutics and heat. Despite extensive research, several limitations prevent its clinical

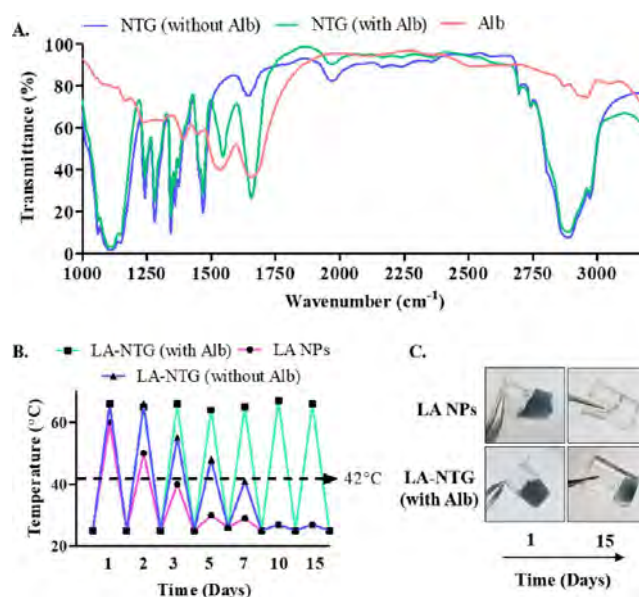


Figure 2. (A) FTIR analysis of NTG (with/without Alb) and Alb alone, (B) sustained photothermal transduction of LA-NTG (with/without Alb) and LA NPs when treated with NIR light (808 nm) for 5 min at different time points (Days). (C) Insets showing residual LA NPs and LA-NTG (with Alb) at day 1 and 15 post NIR light irradiation.

application, such as poor photothermal transduction, repeated dosing, long-term toxicity, and inability to target internal organ tumors (metastasis).³⁸ In order to address these concerns, we have developed a multimodal composite hydrogel based on the combination of Pluronic F-127 (PF), PVA, and albumin (Alb), termed as the nanotransforming hydrogel (NTG) in the current study. The prepared hydrogel samples exhibited sol–gel and gel–sol transition when sequentially exposed to 4°C , 37°C , and vice versa (Figure S1). However, the gel–sol transition of the NTG was altered when it was exposed to 60°C . This alteration could have been due to the presence of albumin in the hydrogel matrix. It is reported that when albumin is exposed to higher temperatures, it exhibits changes in protein folding resulting in cross-linking.^{39,40} In order to impart NIR responsiveness to this hydrogel, hybrid liposomal gold nanoparticles (LA NPs) were later incorporated (LA-NTG) (Figure 1A–D). The UV–Vis spectrometric analysis revealed that the LA NPs exhibited a broad range of NIR absorbance, peaking at 808 nm (Figure S2A). To evaluate the photothermal transduction efficacy of LA NPs, the nanoparticles were irradiated with 808 nm NIR laser (650 mW). When the LA-NTG was irradiated with NIR light, localized hyperthermia was achieved with the temperature reaching $>55^\circ\text{C}$ by the end of 5 min of irradiation (Figure 1C, S2B), rendering LA-NTG as photothermally active.

The prepared gels were then subjected to SEM imaging for evaluating the surface morphology. The NTG sample that was exposed to 60°C showed a prominent cross-linking behavior, while no such cross-linking pattern was observed in control samples (Figure 1E). Similarly, LA-NTG being NIR responsive displayed a similar cross-linking pattern when irradiated with NIR light, suggesting NIR light-mediated gelation (Figure 1F). At the same time, no such cross-linking was seen in nonirradiated samples. This confirmed that the presence of albumin in the gel matrix was responsible for altering the gel–sol transition of LA-NTG.

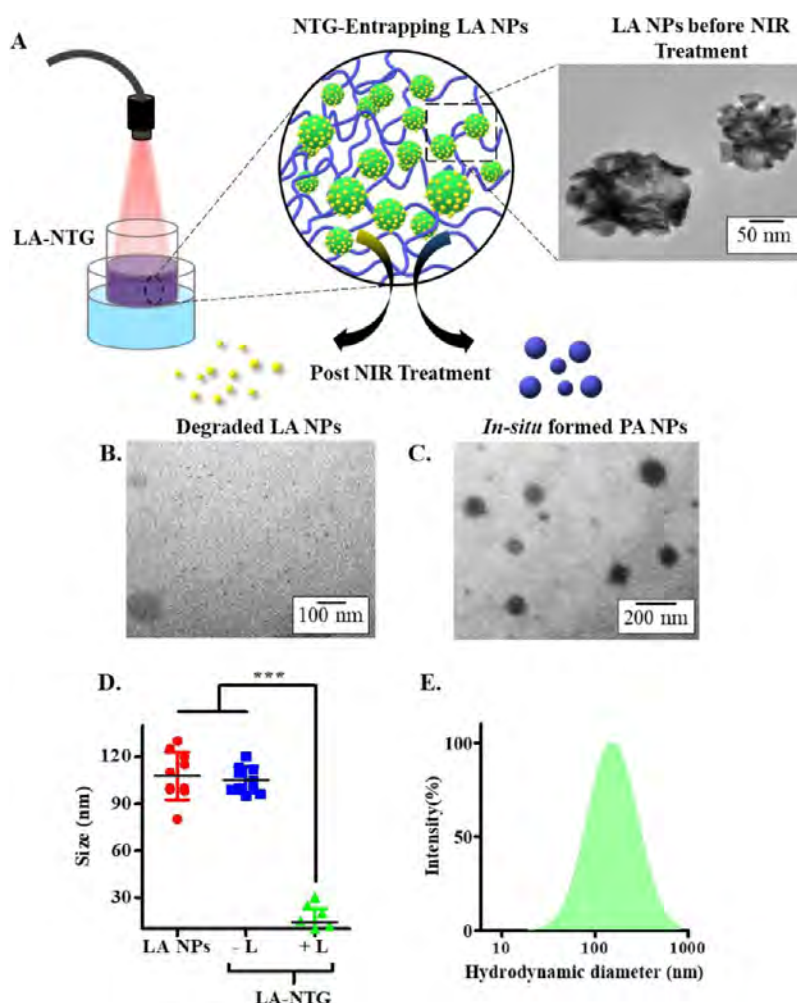


Figure 3. (A) Schematic representation of NTG entrapping LA NPs before and after NIR treatment; the TEM image shows intact LA NPs in the gel matrix before NIR light treatment. (B & C) TEM imaging of disintegrated LA NPs post NIR light treatment and *in situ* formed PA NPs released from LA-NTG (image from the same sample showing both degraded LA NPs and PA NPs in the same field). (D) Size analysis of LA NPs in water and the LA-NTG matrix before and after NIR light irradiation. One-way ANOVA was performed followed by Post-Hoc Tukey's test (***) $P < 0.001$. Data are represented as mean \pm SD. (E) DLS analysis of PA NPs released from NTG (with Alb).

Later rheological studies were conducted with LA-NTG (with/without Alb) to evaluate the influence of albumin on the viscosity of the hydrogel. Both the gel samples exhibited minimal viscosity at 4 °C with similar phase transitions (~ 21 °C), which is essential for injectability (Figure 1G). However, when the gel samples were incubated at 37 °C, a steady increase in the viscosity of the samples was noted. Among both, the gel sample LA-NTG (with Alb) exhibited higher viscosity. Additionally, the effect of thermal cross-linking (60 °C) on the viscosity of gel samples was evaluated by the reverse thermal sweep test. The LA-NTG (with Alb) maintained enhanced viscosity for 20 min and displayed a decline in viscosity at ~ 16 °C, whereas LA-NTG (without Alb) showed a decrease in viscosity at ~ 20 °C (Figure 1H). The viscosity of LA-NTG (with Alb) remained higher at 4 °C (i.e., 9600 Pa·s) when compared with LA-NTG (without Alb) (i.e., 4260 Pa·s). The changes observed in the rheological property further confirm the cross-linking of LA-NTG (with Alb) when exposed to elevated temperatures.

The hydrogels were further characterized by FT-IR spectroscopy. The characteristic bands displayed by Pluronic are 1250–1000 cm^{-1} (C–O–C stretching and CH_2 rocking vibrations), 2975 cm^{-1} (C–H stretching vibration of PEO segments), and 1730 cm^{-1} (C=O stretching),⁴¹ whereas PVA shows 3280

cm^{-1} (OH stretching), 2917 cm^{-1} (CH_2 asymmetric stretching), 1690 cm^{-1} (C=O carbonyl stretching), 1425 cm^{-1} (CH_2 bending), 1324 cm^{-1} (C–H deformation), 1081 cm^{-1} (C–O stretching), and 839 cm^{-1} (C–C stretching).⁴² Albumin exhibits 3439 cm^{-1} (–OH stretching), 1651 cm^{-1} (C=O stretching), 1531 cm^{-1} (N–H vibration), and 1367 cm^{-1} (C–N vibration).⁴³ The FT-IR spectrum of the NTG (with Alb) displayed all the characteristic peaks of PVA, PF, and Alb, suggesting the formation of a physical gel²⁴ (Figure 2A).

The LA-NTG was then tested for its photothermal stability. As shown in (Figure 2B), LA-NTG (with Alb) exhibited a sustained photothermal effect, which lasted for 15 days, while LA-NTG (without Alb) and LA NPs showed it for <7 and <5 days, respectively (Figures 2B and S3). As the LA-NTG (with Alb) formed a stable depot, the photothermal transducer (LA NPs) was retained within the matrix for longer durations as opposed to LA-NTG (without Alb) or LA NPs alone (Figures 2C and S3). Thus LA-NTG (with Alb) displayed sustained photothermal transduction on multiple NIR light irradiation. Taken together, these findings demonstrated that LA-NTG (with Alb) could be employed as a promising candidate for sustained PTT without the need for repeated injections. Thus,

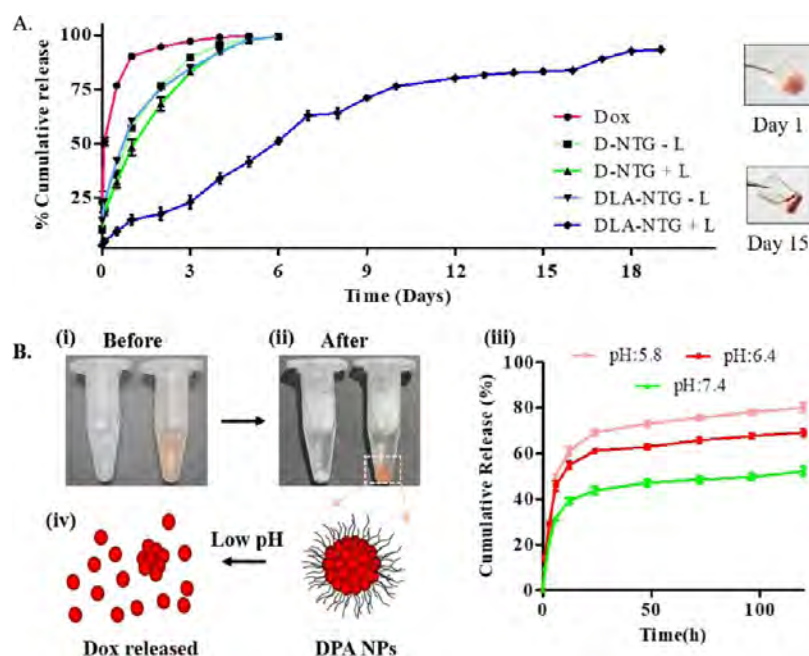


Figure 4. (A) NIR light triggered cumulative drug release from DLA-NTG, insert shows the DLA-NTG at day 1 and day 15 showing remnant hydrogel. [B(i,ii)] Isolated PA NPs and DPA NPs (Dox entrapping PA NPs) before and after centrifugation showing pellet formation. (iii,iv) Dox release kinetics from DPA NPs when suspended at varying pH 5.8, 6.4, and 7.4, and schematic representing the drug release. Data are represented as mean \pm SD ($n = 3$).

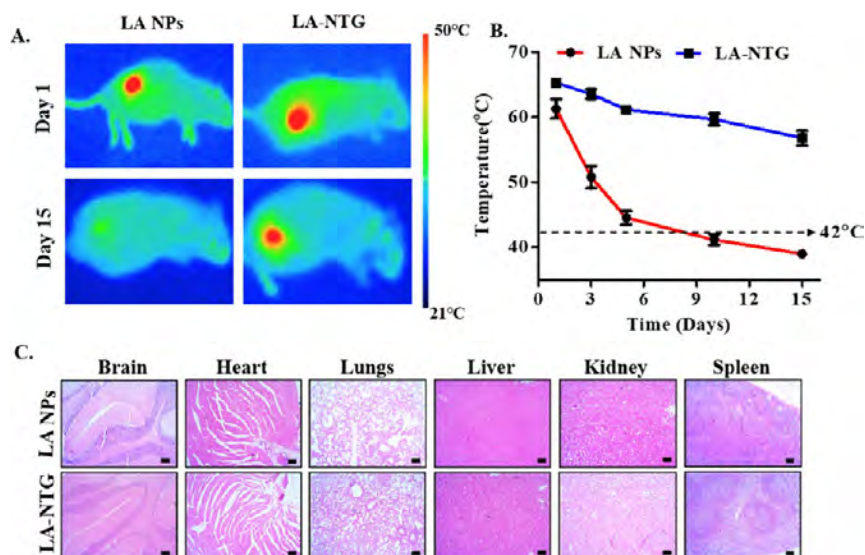


Figure 5. (A) *In vivo* photothermal imaging of LA NPs and LA-NTG injected mice exhibiting sustained photothermal transduction. (B) Photothermal transduction efficacy of LA NPs and LA-NTG till 15 days' post injection ($n = 3$). Data are represented as mean \pm SD. (C) Histopathological evaluation of the isolated organs (brain, heart, lungs, liver, kidneys, and spleen) from LA NPs and LA-NTG administered mice respectively post 15 days.

all the studies conducted henceforth were performed using LA-NTG (with Alb) denoted as LA-NTG.

A wide variety of photothermal transducers have been employed for chemo-PTT, particularly metallic nanoparticles like gold nanorods, nanostars, or metal nanoflakes.^{44–46} These nanosystems exhibit poor elimination profiles from the biological system and thus render them ineffective in a clinical setting. The LA NPs employed in the current study exhibits significant advantage over other metallic systems, as it is known to undergo NIR light-mediated disintegration.¹⁹ Having LA NPs entrapped within the gel matrix, a sustained photothermal effect is achieved, as demonstrated earlier. In conjunction with it, *in*

situ disintegration of LA NPs can also be performed due to repeated NIR light irradiation within the gel matrix (Figure 3A). The fate of LA NPs entrapped in the LA-NTG was evaluated by performing TEM imaging of samples retrieved from hydrogels following repeated NIR light irradiation. The disintegrated gold nanostructure <10 nm was evident, as shown in Figures 3B,D and S4A, confirming the NIR light-mediated disintegration of entrapped LA NPs. The disintegration of the gold coating of LA NPs into <10 nm particles can enhance the rate of clearance from the biological system, which is an essential element for clinical application.^{19,47}

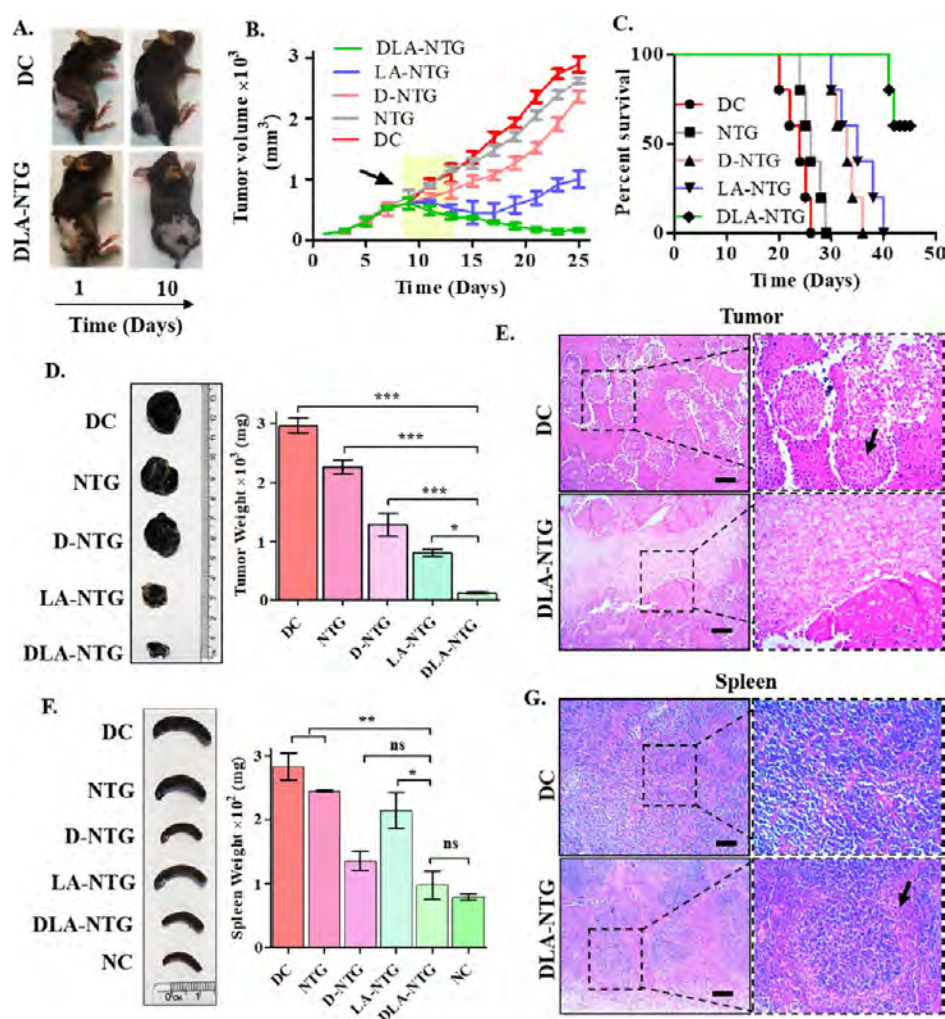


Figure 6. (A) Representative images showing tumor regression of animals treated with a single dose of DLA-NTG by synergistic chemo-PTT. (B) Tumor volumes of the animals during treatment (black arrow shows initiation of treatment, and yellow-shaded area shows the duration of the treatment). Data are represented as mean \pm SD ($n = 5$). (C) Percentage survival of animals treated with NTG, D-NTG, LA-NTG, DLA-NTG, and disease control. (D) Representative images showing isolated tumors post treatment and weight of the tumors. (E) H/E staining of isolated tumor sections imaged in 4 \times and 10 \times . (F) Representative images showing isolated spleens and weight of the organ. (G) H/E staining of isolated spleens. One-way ANOVA was performed followed by Post-Hoc Tukey's test (* $P < 0.05$, ** $P < 0.01$, *** $P < 0.001$).

Interestingly, the TEM imaging of LA-NTG also revealed the presence of *in situ*-formed PA NPs released from LA-NTG along with disintegrated gold nanostructures. These PA NPs were within the range of 100–150 nm (Figures 3C and S4A). The formation of PA NPs was also confirmed by performing DLS analysis on the aliquots retrieved from NTGs. As shown in Figure 3E, the NTG showed the particles of mean size ~ 120 nm, when compared with the respective control (~ 48.5 nm) (Figure S4D,E). These findings are in corroboration with TEM analysis suggesting the *in situ* formation of PA NPs from NTG/LA-NTG. Based on these findings, we propose that the passive disintegration of LA-NTG has led to the emergence of PA NPs, thus displaying nanotransformation from a hydrogel depot to PA NPs (Figure S4A–C). This transition can be of significant importance in targeting the metastasized secondary tumors by constantly releasing PA NPs from LA-NTG.

The LA-NTG was then evaluated for NIR laser-mediated drug release, for which Dox was used as a model drug. It was observed that in DLA-NTG, about $84.7 \pm 0.52\%$ of Dox was released by the end of 72 h when compared to $97.2 \pm 0.6\%$ in free Dox. Interestingly, DLA-NTG showed a remarkable

transition in the drug release profile, when the gel samples were irradiated with NIR light. It was observed that $83.26 \pm 0.2\%$ Dox was released by the end of the 15th day (360 h) and lasted till the 18th day (Figure 4A). The sustained drug release exhibited by (DLA-NTG + L) was attributed to the stable depot formed by photothermal cross-linking. A similar trend of drug release was observed when Dox was entrapped in LA NPs embedded in NTGs (Figure S5A). It is well reported that the primary cause of cancer relapse is the residual cancer cells that form the foci for regrowth.^{48,49} Thus, to effectively counter the cancer relapse, it is essential to suppress residual cancer cells' growth.⁵⁰ As with our findings, the NIR light-mediated photothermal cross-linking of DLA-NTG can significantly inhibit tumor growth primarily by localized PTT and later suppress cancer cells' regrowth by releasing Dox for a prolonged duration of time.

We have then evaluated the Dox entrapment within the *in situ*-formed PA NPs. The D-NTG hydrogel was dissolved, and the PA NPs were isolated by centrifugation. The pellet formed showed the presence of Dox within the PA NPs with an entrapment efficiency of $47 \pm 3\%$ (Figure 4B,ii). These DPA

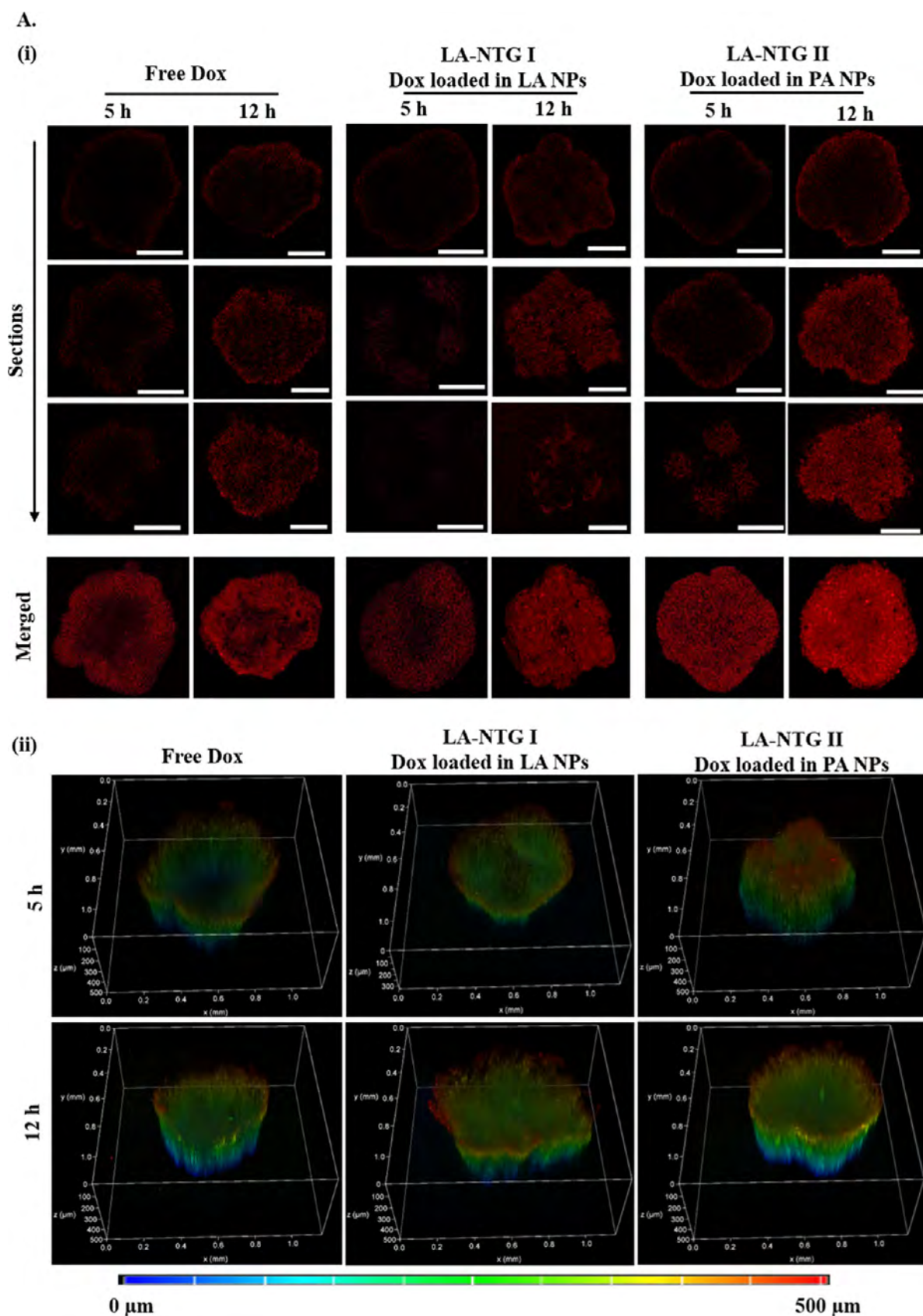


Figure 7. (A(i)) Representative images showing the intracellular uptake of free Dox, LA-NTG I (drug loaded in LA NPs), and LA-NTG II (drug loaded in PA NPs) in 3D cancer cell spheroids at 5 and 12 h time points (scale bar: 250 μm). (ii) Depth mapping of the intracellular uptake in the treated spheroids.

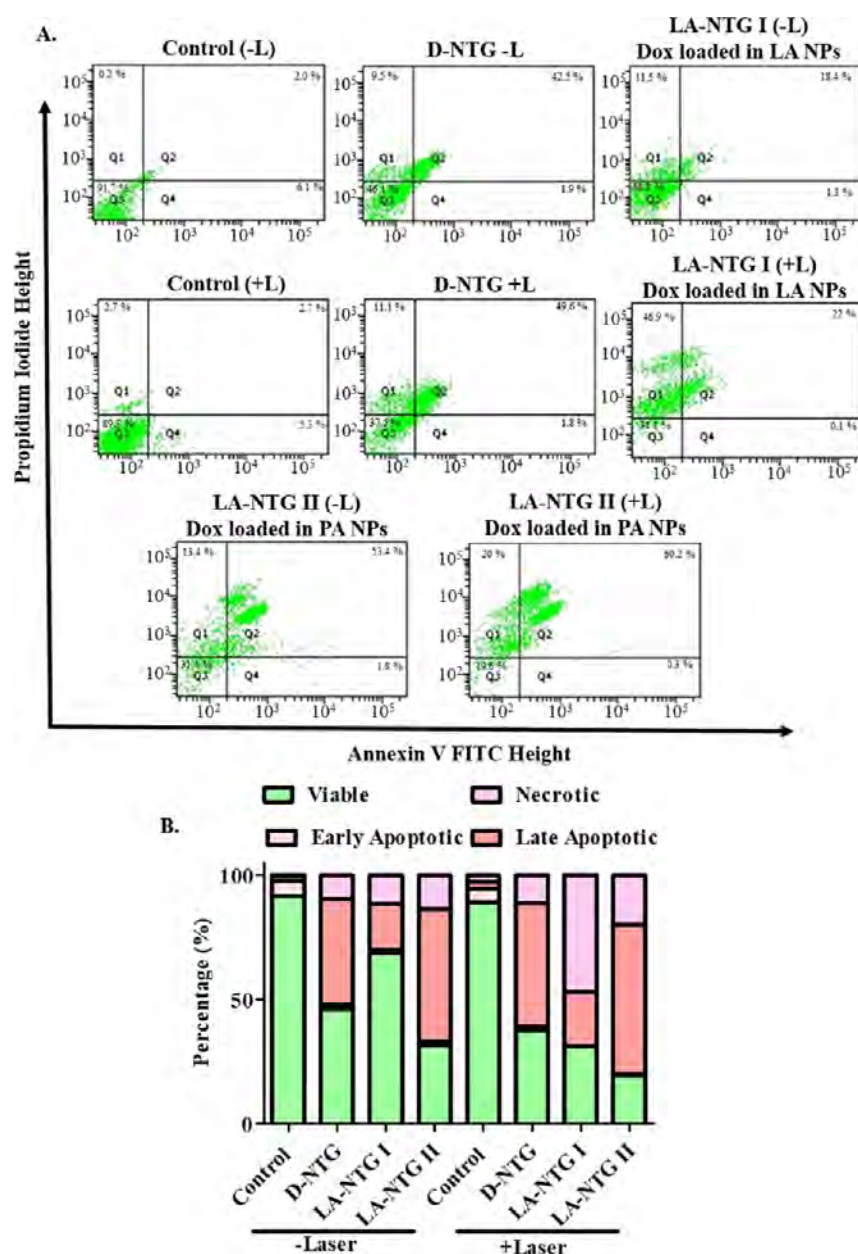


Figure 8. (A) NIR laser-mediated cell cytotoxicity analysis by flow cytometry using annexin V FITC and propidium iodide of the following groups: control, D-NTG, LA-NTG I (drug loaded in LA NPs), and LA-NTG II (drug loaded in PA NPs). Q1: necrotic cells (A+), Q2: late apoptotic cells (A+), Q3: Viable cells (A-), and Q4: early apoptosis (A+). (B) Graph representing the mean percentage values of apoptotic and necrotic cells.

NPs were then subjected to drug release studies in varying pH. The DPA NPs showed a pH-responsive release with about ~80, ~70, and ~50% of Dox released within 120 h at pH 5.8, 6.4, and 7.4, respectively (Figure 4Biii,iv). These findings confirmed that the *in situ*-formed PA NPs could entrap not only the drug but also exhibit a pH-responsive release. The pH responsiveness of PA NPs could hold significant importance in inhibiting aggressive metastatic tumors as they are known to have an acidic microenvironment.⁵¹ Delivering the chemotherapeutic agents to metastasized tumors combined with pH-based drug release can be an effective therapeutic strategy for inhibiting metastasis. In the current study, the biocompatibility of hydrogels was evaluated in NIH 3T3, and it was found to be completely biocompatible (Figure S5).

The LA-NTG was then evaluated for *in vivo* sustained photothermal transduction efficacy. The animals injected with

only LA NPs exhibited a decline in localized photothermal transduction from ~60 to ~45 °C by the end of the 5th day, suggesting clearance of LA NPs from the injected site. However, in LA-NTG, a sustained photothermal effect was observed with the temperature reaching up to >55 °C by the end of the 15th day (Figures 5A,B, S6A–C). These findings confirm the *in vivo* sustained photothermal transduction of LA-NTG at the injected site, thus reducing the need for multiple injections required for treatment. Furthermore, no signs of toxicity were observed in histopathological studies of the isolated organs, confirming the biocompatible nature of the smart hydrogel (Figure 5C). The *in vitro* synergistic chemo-photothermal effect was evaluated on B16F10 cell lines, and it was observed that DLA-NTG was able to elicit significant cancer cell death (Figure S7A,B). Taken together, these findings suggest that LA-NTG can be used as a

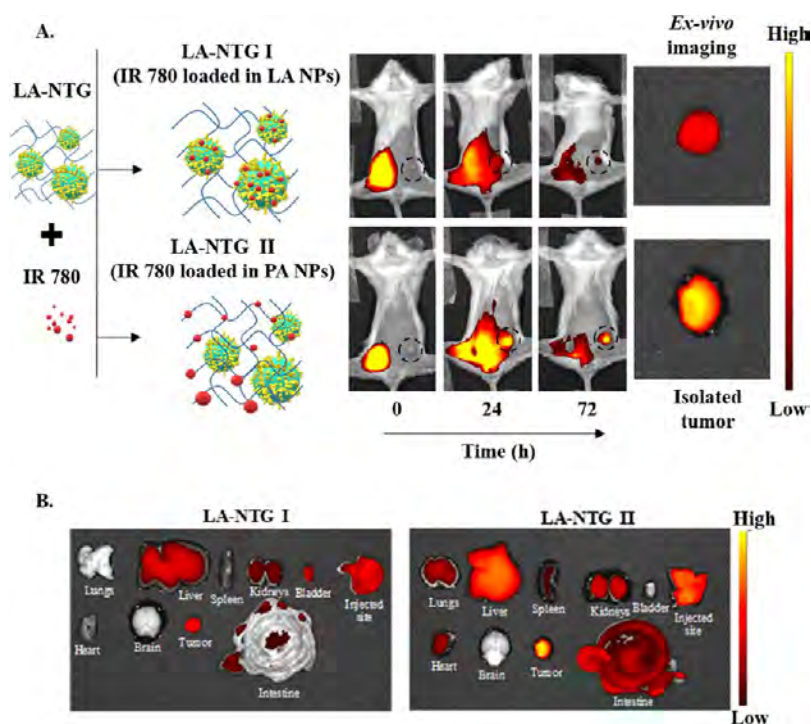


Figure 9. (A) Single tumor targeting by LA-NTG I (dye loaded in LA NPs) and LA-NTG II (dye loaded in PA NPs). (B) *Ex-vivo* imaging of isolated organs treated with LA NTG I and LA NTG II.

promising therapeutic modality for the treatment of localized tumors by exhibiting sustained chemo-PTT.

The efficacy of DLA-NTG as a sustained photothermal and drug depot was then evaluated *in vivo* by employing the B16F10 cell-induced melanoma mice model. The animals were allowed to attain a tumor size of about $\approx 200 \text{ mm}^3$, following which they were injected with the respective samples. The animals were then subsequently irradiated with laser for a total of 3 days with a 2 day interval. By the end of the treatment, significant tumor suppression was seen in the group treated with LA-NTG and DLA-NTG due to photothermal and combined chemo-photothermal effects, respectively (Figures 6A,B and S8). The untreated animals (disease control) and only NTG-treated groups exhibited the shortest survival duration (<30 days) among all the groups. In contrast, mice treated with D-NTG, LA-NTG, and DLA-NTG showed an enhanced survival of 35, 40, and >45 days, respectively (Figure 6C). There was a >20-fold decrease in tumors' weight in the DLA-NTG treated group compared with the disease control (Figure 6D). When the isolated tumors were subjected to histopathological studies, it was observed that a characteristic organoid pattern was evident in the disease control group with eosinophilic staining. The growth of these organoid structures radiated from blood vessels, and significant blood vessel compression was also apparent with invasion.⁵² However, in DLA-NTG, a substantial reduction in the tumor load was evident, and enhanced fibroblastic activity was also seen; it could be in response to the localized thermal damage (Figure 6E). These findings confirm the effectiveness of DLA-NTG in curbing the growth of cancer by exhibiting a sustained chemo-photothermal effect. The earlier literature evidence shows that for significant tumor suppression, repeated dosing is needed.⁵³ However, in the current study, tumor suppression was observed with a single dose of DLA-NTG and three cycles of noninvasive NIR light irradiation.

One of the characteristic features of cancer is the immune suppression exerted by a growing tumor, which is known to disrupt homeostasis and immune cell regulation. The spleen plays a vital role in maintaining immunity and maintains homeostasis. It is reported that in cancer, spleen enlargement is usually correlated with the extent of cancer burden and its systemic side effects.^{54,55} Thus, phenotypic changes in the spleen can provide insights into disease progression and cancer severity.⁵⁶ A positive correlation was observed between spleen enlargement and tumor growth, as shown in Figure 6F. A three-fold increase in the spleen size and weight was seen in untreated mice when compared with normal mice. The tumor-bearing mice treated with NTG + L, LA-NTG + L, and disease control showed similar spleen enlargement. These findings suggest that though PTT effectively suppresses cancer at a localized site, it is incapable of evoking a systemic response or inhibit metastasis. Tumor-bearing mice treated with D-NTG exhibited a relatively normal-sized spleen when compared with disease control. This suggests that sustained release of Dox from D-NTG could have elicited a systemic response but failed in suppressing the localized tumor. Nonetheless, tumor-bearing mice treated with DLA-NTG + L showed a remarkable systemic response besides suppressing the localized tumor. Furthermore, the micro-architecture of the spleen was significantly altered with extensively disorganized white pulp and poor demarcation between white and red pulp in disease control. The DLA-NTG + L-treated group exhibited relatively a normal spleen micro-structure with distinctive red/white pulp and mantle zones (Figure 6G). These results confirm that DLA-NTG can be effective in suppressing localized tumors and can also evoke a systemic response possibly by sustained release of drug from the DLA-NTG depot.

Chemo-PTT is beneficial in preventing localized cancer recurrence; however, it renders ineffective in preventing distant metastases. As with LA-NTG, which releases *in situ* formed PA

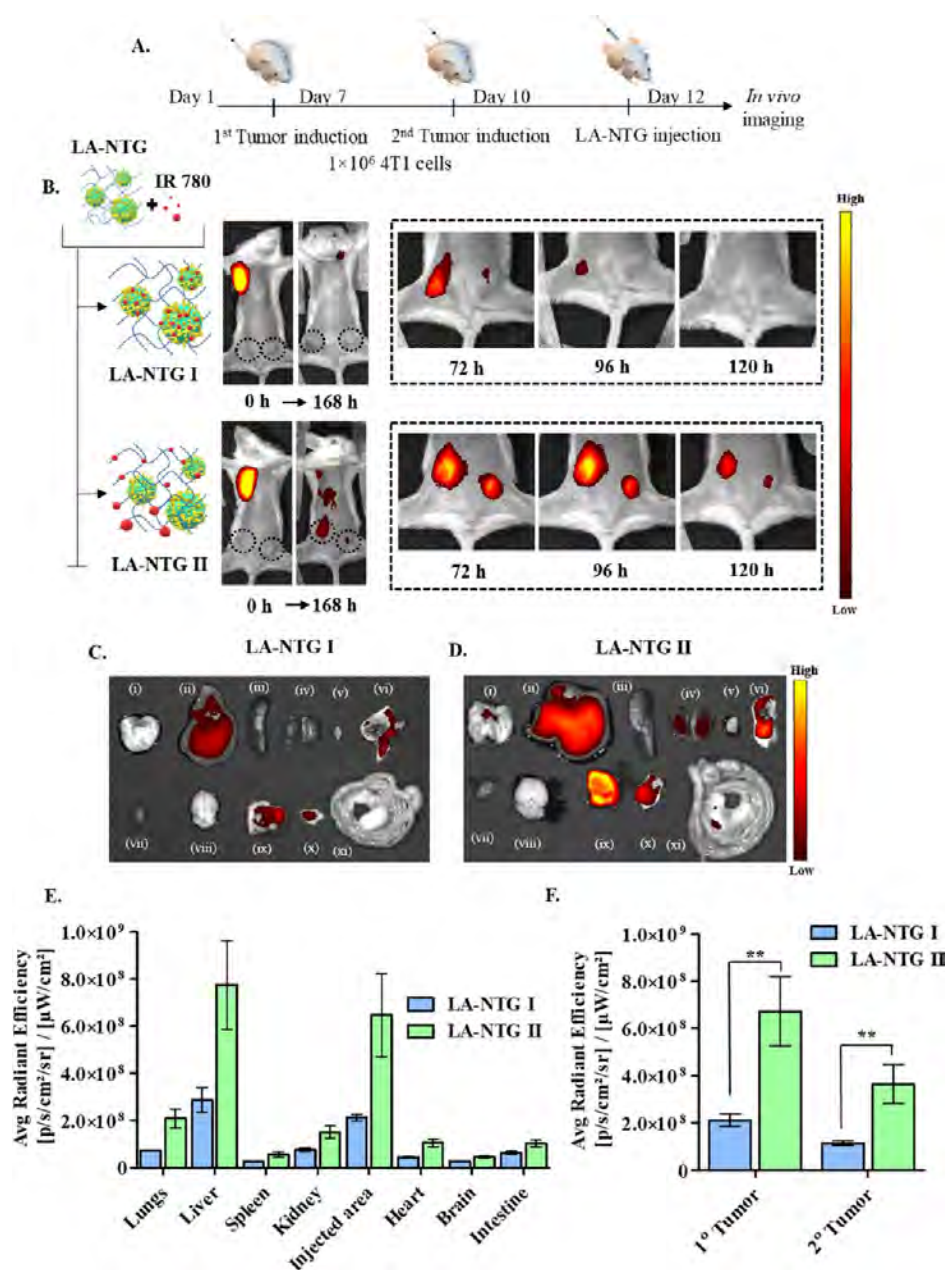


Figure 10. (A) Schematic representation of bilateral orthotropic tumor induction and LA NTG administration. (B) *In vivo* NIR imaging of mice administered with LA-NTG I (dye loaded in LA NPs) and LA-NTG II (dye loaded in PA NPs) and its distant tumor targeting efficacy (C,D) end point *ex-vivo* imaging of isolated organs. ((i) Lungs, (ii) liver, (iii) spleen, (iv) kidney, (v) bladder, (vi) injected sites, (vii) heart, (viii) brain, (ix) primary tumor, (x) secondary tumor, (xi) intestine). (E, F) Biodistribution and accumulation of LA NPs and PA NPs in different organs and tumors respectively. Data are represented as mean \pm SEM ($n = 3$) and unpaired *t*-test was performed (** $P < 0.01$).

NPs, it is worth exploring if these PA NPs can be localized into tumors at distant sites. In order to evaluate the drug delivery and tumor penetration potential of PA NPs, the 3D cell spheroids were employed, in the current study. Dox was loaded in LA NPs (LA-NTG I) and PA NPs (LA-NTG II), respectively, and compared with free Dox to assess the potential drug carrier. As shown in Figure 7Ai, the PA NPs demonstrated higher penetration than free Dox and LA NPs at both 5 and 12 h time points. The 3D mapping of the treated spheroids revealed deeper penetration of PA NPs into the core when compared to the respective controls (Figure 7Aii). The drug uptake was further quantified by subjecting the treated spheroids through flow cytometric analysis. As shown in Figure S9, the spheroids

treated with PA NPs showed higher drug uptake ($\sim 71.5\%$) when compared with LA NPs ($\sim 49\%$). These findings suggest that drug-loaded PA NPs released from LA-NTG can deliver the drug to the core of the tumors, thereby exhibiting deep tumor penetration.

Furthermore, the mode of cell death induced by drug-loaded PA NPs and LA NPs was assessed using annexin V-FITC and propidium iodide probes. As shown in Figure 8A,B, LA-NTG I and LA-NTG II showed 1.3 and 1.8% early apoptosis, 18.4 and 53.4% late apoptosis, and 11.5 and 13.4% necrotic death, respectively. After 5 min of laser irradiation, LA-NTG I and LA-NTG II showed 0.1 and 0.3% early apoptosis, 22 and 60.2% late apoptosis, 46.9 and 20% necrotic death, respectively. The NIR

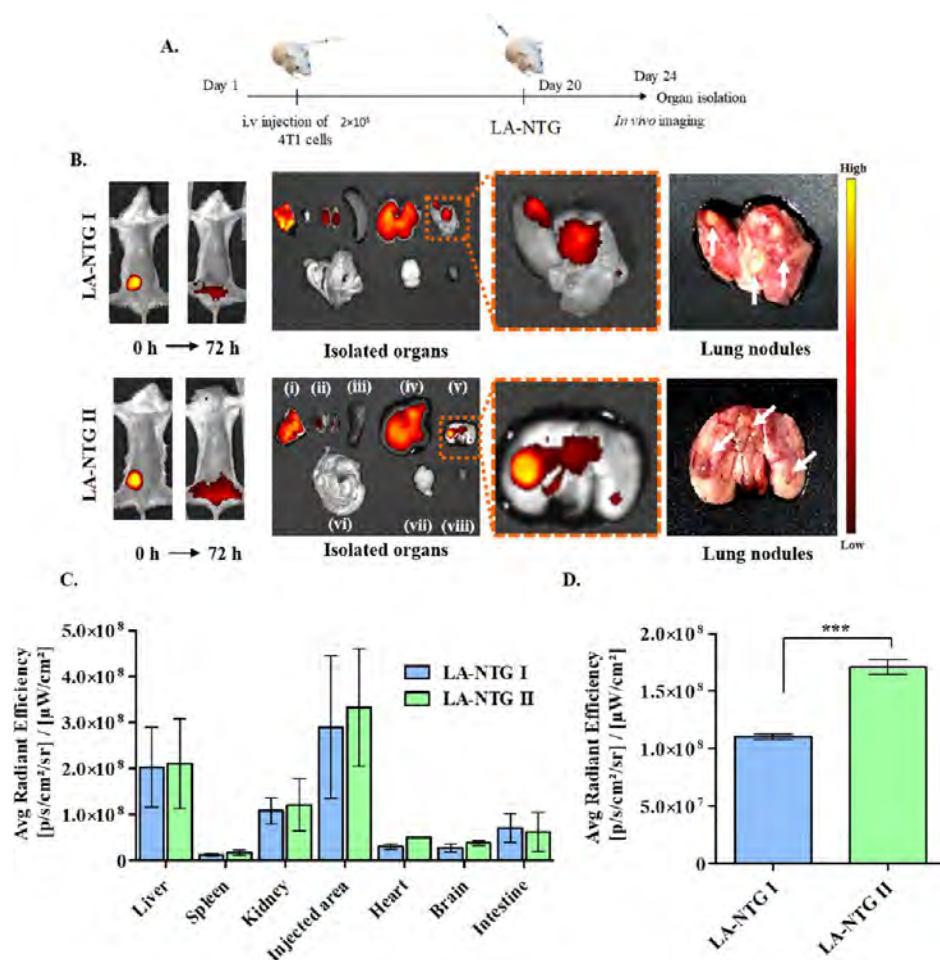


Figure 11. (A) Schematic representation of lung metastasis induction and LA-NTG administration. (B) Metastatic lung nodule targeting by LA-NTG I and LA-NTG II. (i) Skin, (ii) kidneys, (iii) spleen, (iv) liver, (v) lungs, (vi) intestines, (vii) brain, and (viii) heart. (C) Biodistribution of LA NPs and PA NPs in different organs. (D) Quantification of the fluorescent signal from isolated lung nodules (images were acquired from stage B of *in vivo* imaging system). Data are represented as mean \pm SEM ($n = 3$), and unpaired *t*-test was performed (*** $P < 0.001$).

light-triggered LA-NTG II showed higher apoptotic cell death when compared to the LA-NTG I hydrogel. More interestingly, LA-NTG II showed a significant cell death even without NIR light irradiation possibly due to the release of PA NPs. This suggests that PA NPs released from LA-NTG II can be employed to inhibit tumors even without NIR light irradiation.

We then analyzed the biodistribution of LA NPs and PA NPs by using the *in vivo* fluorescence imaging system. A NIR tracker dye (IR 780 iodide) was loaded within LA NPs and PA NPs in LA-NTG I and LA-NTG II, respectively. The fluorescence intensity of the skin samples from injected animals was observed for >10 days in LA-NTG I and LA-NTG II groups, suggesting the gel retention at the injected site for an extended duration *in vivo* (Figure S10). These results were in line with the earlier findings demonstrating sustained photothermal transduction following a single administration (Figure S6B). As the LA-NTG II undergoes nanotransformation into PA NPs, the biodistribution of PA NPs was also noted in all the other organs. The PA NPs exhibited prolonged circulation, as evidenced by the fluorescence signal arising from the heart, lungs, spleen, and liver until five days (Figure S8). Interestingly, the blood samples retrieved from the LA-NTG II-injected group demonstrated enhanced bioavailability for ~ 5 days compared with LA-NTG I. Taken together, these findings indicate that PA NPs can exhibit

prolonged blood circulation and can target internal organs efficiently.

As the PA NPs released from LA-NTG II showed prolonged systemic circulation, we further investigated their ability to target tumors passively at the distant site. The LA-NTG II group exhibited a significant accumulation of PA NPs within the tumor region for 72 h when compared to LA NPs from LA-NTG I (Figures 9A, S11). It was also observed that the accumulation of PA NPs from LA-NTG II showed higher signals from the isolated tumors when compared to LA-NTG I (Figure 9B). These findings further confirm that the PA NPs released from LA-NTG II exhibit prolonged circulation and selective accumulate within the tumor by the EPR effect.⁵⁷

Further, we have also evaluated the accumulation of PA NPs in the bilateral tumor model, Figure 10A. The mice bearing bilateral tumors were injected with LA-NTG I and LA-NTG II in respective groups. The two groups were then imaged to track the localization of nanoparticles (LA NPs and PA NPs). In the LA-NTG I injected group, the LA NPs could localize in the fully developed tumors starting from 12 h post-injection to 96 h (Figures 10B–E, S12). At the same time, localization in the second tumor was minimal. In the LA-NTG II injected group, the PA NP accumulation within the tumor was observed from 12 h post-injection to 120 h. The fluorescence intensity from LA-NTG II was ~ 3.5 fold higher than LA-NTG I in primary tumors

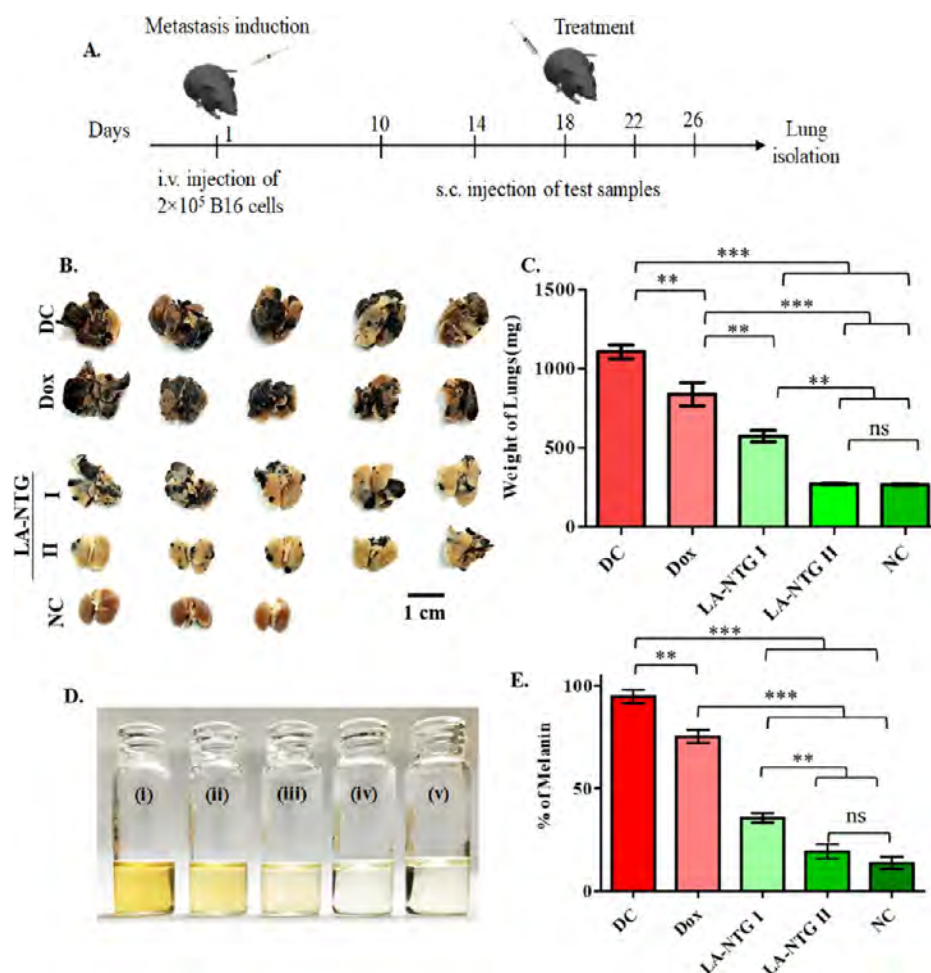


Figure 12. (A) Schematic representation of spontaneous metastasis induction and treatment by LA-NTG; (B) isolated lungs representing lung nodules. (C) Weight of isolated lungs from animals treated with Free Dox, LA-NTG I (Dox loaded LA NPs), LA-NTG II (Dox loaded PA NPs), disease control and normal control. Data are represented as mean \pm SD ($n = 5$). (D,E) Melanin extracted and its quantification from lungs exhibiting melanoma nodules post treatment. (i) Disease control, (ii) Dox, (iii) LA NTG I, (iv) LA NTG II and (v) normal control. Data are represented as mean \pm SD ($n = 5$). One-way ANOVA was performed followed by Post-Hoc Tukey's test (* $P < 0.05$, ** $P < 0.01$, *** $P < 0.001$).

and ~ 3.1 fold in secondary tumors (Figure 10F). These findings strongly suggest that PA NPs released from LA-NTG II could significantly enhance the accumulation of drugs within tumors owing to enhanced tumor permeation and retention.

The metastasis of cancer to multiple organs often presents challenges in the treatment by conventional therapies. Due to the dense tumor matrix and multiple tumor nodules, the chemotherapeutic agent's delivery is restricted. In this study, we have further investigated the ability of PA NPs to target multiple lung metastatic nodules. The schematic Figure 11A shows the study design. The mice were subcutaneously administered to respective groups with LA-NTG I and LA-NTG II in the lower-left flange region. As shown in Figure 11A,B, these groups were then imaged. The isolated lungs of LA-NTG II showed significantly higher and specific fluorescence signals from multiple lung nodules by the end of 72 h. PA NPs showed ~ 1.2 fold enhancement in tumor-targeting than LA NPs, Figure 11C,D. These findings suggest that the prolonged circulation of PA NPs resulted in their accumulation in metastatic lung nodules, demonstrating their ability to target metastatic nodules efficiently. Research studies have attempted to target lung metastasis by employing tumor-targeting peptides like RGD.^{58–60} However, the tumor accumulation and residence time of the earlier reported nanosystems were significantly less.

Lastly, we have evaluated the therapeutic effect of LA-NTG II (PA NPs) on the spontaneous metastasis model. Following the establishment of lung metastasis of B16 melanoma cells, the animals were injected with LA-NTG I (LA NPs), LA-NTG II (PA NPs), free Dox, and saline to their respective groups (Figure 12A). By the end of the study period, there was significant suppression of metastatic lung nodules formed in LA-NTG I- and LA-NTG II-treated groups compared to Dox-treated and disease control groups (Figure 12B). The substantial inhibition of lung nodules in the LA-NTG II group was attributed to the release of PA NPs from the injected site, which accumulated within the tumor nodules and released the drug. The lung weight also confirmed this, where the untreated mice showed ~ 5 fold increase in the weight of lungs compared to the normal control (Figure 12C). However, the Dox-treated group showed a minimal decline in lung weight compared to disease control.

Melanin plays an essential role in alleviating cell stressors. However, excessive melanogenesis in melanoma has shown to be a significant constituent for causing cancer cell resistances toward radiation therapy.^{61,62} By inhibiting the metastasis of melanoma, one can prevent excessive accumulation of melanin in the lungs, thereby rendering the tumor nodules sensitive to radiation therapy. Melanin was also quantified from the isolated lungs. It was observed that the LA-NTG II-treated group

showed minimal melanin compared to disease control and Dox-treated groups (Figure 12D,E), suggesting the inhibition of metastasis and possible radiation sensitization. Lastly, the mice treated with LA-NTG I and LA-NTG II were evaluated for serum markers like AST, ALT, and ALP to assess the disease burden. In the LA-NTG II-treated mice, the levels of these markers were near the normal range (Figure S13). All in all, these findings confirmed the therapeutic efficacy of the nanotransforming gel as a promising agent for localized chemo-PTT and for inhibiting metastasis.

4. CONCLUSIONS

In this study, we report a biocompatible and biodegradable NIR-responsive smart *in situ* nanotransforming gel. The injected hydrogel depot degrades into self-stabilized polymeric albumin nanoparticles (PA NPs), exhibiting prolonged systemic circulation and accumulation in distant tumors by the EPR effect. These PA NPs were also able to accumulate within the secondary metastatic lung nodules selectively for a prolonged time. When tested *in vivo* on melanoma-bearing mice, a single dose of hydrogel inhibited the tumor growth by demonstrating sustained chemo-PTT. It was also able to prevent splenomegaly, thereby reducing cancer burden. When tested *in vivo*, spontaneous metastasis model LA-NTG was also able to suppress the formation of metastatic lung nodules, outperforming chemotherapy. Thus, the protein-polymer-based nanotransforming gels hold immense potential for clinical translation and can offer a better therapeutic effect in treating aggressive cancers.

■ ASSOCIATED CONTENT

Supporting Information

The Supporting Information is available free of charge at <https://pubs.acs.org/doi/10.1021/acsami.1c17054>.

UV–Vis spectroscopic analysis, photothermal transduction, sol–gel and gel–sol, dissolution studies, TEM imaging, biocompatibility, *in vivo* photothermal transduction, *ex vivo* bio distribution analysis, *in vivo* single tumor targeting, *in vivo* double tumor targeting, *in vitro* cytotoxicity, 2D cytotoxicity evaluation, 3D intracellular uptake, *in vivo* tumor monitoring, and serum parameters (PDF)

■ AUTHOR INFORMATION

Corresponding Author

Aravind Kumar Rengan — Department of Biomedical Engineering, Indian Institute of Technology Hyderabad, Hyderabad, Telangana 502285, India; orcid.org/0000-0003-3994-6760; Email: aravind@bme.iith.ac.in

Authors

Syed Baseeruddin Alvi — Department of Biomedical Engineering, Indian Institute of Technology Hyderabad, Hyderabad, Telangana 502285, India

Rajalakshmi P S — Department of Biomedical Engineering, Indian Institute of Technology Hyderabad, Hyderabad, Telangana 502285, India

Nazia Begum — Department of Pharmacology, G. Pulla Reddy College of Pharmacy, Hyderabad, Telangana 500028, India

Anil Bankati Jogdand — Department of Biomedical Engineering, Indian Institute of Technology Hyderabad, Hyderabad,

Telangana 502285, India; orcid.org/0000-0001-7477-0276

Bantal Veeresh — Department of Pharmacology, G. Pulla Reddy College of Pharmacy, Hyderabad, Telangana 500028, India

Complete contact information is available at:

<https://pubs.acs.org/doi/10.1021/acsami.1c17054>

Author Contributions

#S.B.A. and R.P.S. contributed equally. S.B.A.: material preparation, experimental design, experimental work, *in vivo* analysis, and manuscript writing; R.P.S.: material preparation, experimental design, experimental work, *in vivo* analysis, manuscript writing N.B.: *in vivo* analysis, A.J.: review B.V.: *in vivo* analysis and review, A.K.R.: experimental design, manuscript preparation, and review.

Notes

The authors declare no competing financial interest.

■ ACKNOWLEDGMENTS

The authors would like to acknowledge the following funding agencies: DBT-IYBA (BT/09/IYBA/2015/14), MHRD IMPRINT 1 and 2 (4291, 00275), DST INSPIRE (INSPIRE/04/2015/00037), (DST/TDT/AMT/2017/227), and Vasudha Foundation, CRG/2020/005069. The authors would like to acknowledge Lipoid Germany and VAV Pvt Ltd for providing a generous sample of lipid. Author S.B.A. would like to thank the CSIR for SRF as financial support (09/1001(0044)/2019-EMR-1), and RJ would like to acknowledge the UGC (938/(OBC) (CSIR-UGC NET Dec.2016)) for financial support.

■ REFERENCES

- (1) Siegel, R. L.; Miller, K. D.; Jemal, A. Cancer statistics, 2019. *Ca-Cancer J. Clin.* **2019**, *69*, 7.
- (2) Eccles, S. A.; Welch, D. R. Metastasis: Recent Discoveries and Novel Treatment Strategies. *Lancet* **2007**, *369*, 1742–1757.
- (3) Barker, H. E.; Paget, J. T. E.; Khan, A. A.; Harrington, K. J. The Tumour Microenvironment after Radiotherapy: Mechanisms of Resistance and Recurrence. *Nat. Rev. Cancer* **2015**, *15*, 409–425.
- (4) Zhang, W.; Ji, T.; Li, Y.; Zheng, Y.; Mehta, M.; Zhao, C.; Liu, A.; Kohane, D. S. Light-Triggered Release of Conventional Local Anesthetics from a Macromolecular Prodrug for on-Demand Local Anesthesia. *Nat. Commun.* **2020**, *11*, 2323.
- (5) Rwei, A. Y.; Zhan, C.; Wang, B.; Kohane, D. S. Multiply Repeatable and Adjustable On-Demand Phototriggered Local Anesthesia. *J. Controlled Release* **2017**, *251*, 68–74.
- (6) Rwei, A. Y.; Wang, B.; Ji, T.; Kohane, D. S. Predicting the Tissue Depth for Remote Triggering of Drug Delivery Systems. *J. Controlled Release* **2018**, *286*, 55.
- (7) Soengas, M. S.; Lowe, S. W. Apoptosis and Melanoma Chemoresistance. *Oncogene* **2003**, *22*, 3138.
- (8) Suda, K.; Mitsudomi, T. Successes and Limitations of Targeted Cancer Therapy in Lung Cancer. *Prog. Exp. Tumor Res.* **2014**, *41*, 62.
- (9) Attia, M. F.; Anton, N.; Wallyn, J.; Omran, Z.; Vandamme, T. F. An Overview of Active and Passive Targeting Strategies to Improve the Nanocarriers Efficiency to Tumour Sites. *J. Pharm. Pharmacol.* **2019**, *71*, 1185.
- (10) Maeda, H.; Khatami, M. Analyses of repeated failures in cancer therapy for solid tumors: poor tumor-selective drug delivery, low therapeutic efficacy and unsustainable costs. *Clin. Transl. Med.* **2018**, *7*, No. e11.
- (11) Yu, M.; Zheng, J. Clearance Pathways and Tumor Targeting of Imaging Nanoparticles. *ACS Nano* **2015**, *9*, 6655.
- (12) Laurano, R.; Boffito, M. Thermosensitive Micellar Hydrogels as Vehicles to Deliver Drugs With Different Wettability. *Front. Bioeng. Biotechnol.* **2020**, *8*, 708.

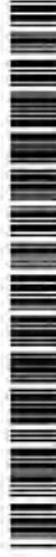
- (13) Xu, C.; Xu, J.; Zheng, Y.; Fang, Q.; Lv, X.; Wang, X.; Tang, R. Active-Targeting and Acid-Sensitive Pluronic Prodrug Micelles for Efficiently Overcoming MDR in Breast Cancer. *J. Mater. Chem. B* **2020**, *8*, 2726.
- (14) Xiao, Y.; Gu, Y.; Qin, L.; Chen, L.; Chen, X.; Cui, W.; Li, F.; Xiang, N.; He, X. Injectable Thermosensitive Hydrogel-Based Drug Delivery System for Local Cancer Therapy. *Colloids Surf., B* **2021**, *200*, 111581.
- (15) Chen, Y.-Y.; Wu, H.-C.; Sun, J.-S.; Dong, G.-C.; Wang, T.-W. Injectable and Thermoresponsive Self-Assembled Nanocomposite Hydrogel for Long-Term Anticancer Drug Delivery. *Langmuir* **2013**, *29*, 3721–3729.
- (16) von Schuckmann, L. A.; Hughe, M. C. B.; Ghiasvand, R.; Malt, M.; van der Pols, J. C.; Beesley, V. L.; Khosrotehrani, K.; Smithers, B. M.; Green, A. C. Risk of Melanoma Recurrence After Diagnosis of a High-Risk Primary Tumor. *JAMA Dermatol.* **2019**, *155*, 688.
- (17) Riggio, A. I.; Varley, K. E.; Welm, A. L. The Lingering Mysteries of Metastatic Recurrence in Breast Cancer. *Br. J. Cancer* **2021**, *124*, 13–26.
- (18) Toczylowska, B.; Zieminska, E.; Goch, G.; Milej, D.; Gerega, A.; Liebert, A. Neurotoxic Effects of Indocyanine Green -Cerebellar Granule Cell Culture Viability Study. *Biomed. Opt. Express* **2014**, *5*, 800.
- (19) Rengan, A. K.; Bukhari, A. B.; Pradhan, A.; Malhotra, R.; Banerjee, R.; Srivastava, R.; De, A. In Vivo Analysis of Biodegradable Liposome Gold Nanoparticles as Efficient Agents for Photothermal Therapy of Cancer. *Nano Lett.* **2015**, *15*, 842–848.
- (20) Ning, X.; Peng, C.; Li, E. S.; Xu, J.; Vinluan, R. D.; Yu, M.; Zheng, J. Physiological Stability and Renal Clearance of Ultrasmall Zwitterionic Gold Nanoparticles: Ligand Length Matters. *APL Mater.* **2017**, *5*, 053406.
- (21) Singh, S. P.; Alvi, S. B.; Pemmaraju, D. B.; Singh, A. D.; Manda, S. V.; Srivastava, R.; Rengan, A. K. NIR Triggered Liposome Gold Nanoparticles Entrapping Curcumin as in Situ Adjuvant for Photothermal Treatment of Skin Cancer. *Int. J. Biol. Macromol.* **2018**, *110*, 375–382.
- (22) Knights-Mitchell, S. S.; Romanowski, M. Near-Infrared Activated Release of Doxorubicin from Plasmon Resonant Liposomes. *Nanotheranostics* **2018**, *2*, 295–305.
- (23) Gioffredi, E.; Boffito, M.; Calzone, S.; Giannitelli, S. M.; Rainer, A.; Trombetta, M.; Mozetic, P.; Chiono, V. Pluronic F127 Hydrogel Characterization and Biofabrication in Cellularized Constructs for Tissue Engineering Applications. *Procedia CIRP* **2016**, *49*, 125–132.
- (24) Bercea, M.; Morariu, S.; Nita, L. E.; Darie, R. N. Investigation of Poly(Vinyl Alcohol)/Pluronic F127 Physical Gels. *Polym. Plast. Technol. Eng.* **2014**, *53*, 1354–1361.
- (25) Baei, P.; Jalili-firoozinezhad, S.; Rajabi-zeleti, S.; Tafazzoli-shadpour, M.; Baharvand, H.; Aghdami, N. Electrically Conductive Gold Nanoparticle-Chitosan Thermosensitive Hydrogels for Cardiac Tissue Engineering. *Mater. Sci. Eng., C* **2016**, *63*, 131–141.
- (26) Chatterjee, S.; Hui, P. C.-L.; Kan, C.-w.; Wang, W. Dual-responsive (pH/temperature) Pluronic F-127 hydrogel drug delivery system for textile-based transdermal therapy. *Sci. Rep.* **2019**, *9*, 1–13.
- (27) Zeng, J.; Shi, D.; Gu, Y.; Kaneko, T.; Zhang, L.; Zhang, H.; Kaneko, D.; Chen, M. Injectable and Near-Infrared-Responsive Hydrogels Encapsulating Dopamine-Stabilized Gold Nanorods with Long Photothermal Activity Controlled for Tumor Therapy. *Biomacromolecules* **2019**, *20*, 3375–3384.
- (28) Du, H.; Li, C.; Luan, Y.; Liu, Q.; Yang, W.; Yu, Q.; Li, D.; Brash, J. L.; Chen, H. An antithrombotic hydrogel with thrombin-responsive fibrinolytic activity: breaking down the clot as it forms. *Mater. Horiz.* **2016**, *3*, 556.
- (29) Martínez-Sanz, M.; Ström, A.; Lopez-Sanchez, P.; Knutsen, S. H.; Ballance, S.; Zobel, H. K.; Sokolova, A.; Gilbert, E. P.; López-Rubio, A. Advanced Structural Characterisation of Agar-Based Hydrogels: Rheological and Small Angle Scattering Studies. *Carbohydr. Polym.* **2020**, *236*, 115655.
- (30) Li, W.; Xue, B.; Shi, K.; Qu, Y.; Chu, B.; Qian, Z. Magnetic Iron Oxide Nanoparticles/10-Hydroxy Camptothecin Co-Loaded Nanogel for Enhanced Photothermal-Chemo Therapy. *Appl. Mater. Today* **2019**, *14*, 84–95.
- (31) Park, Y. I.; Kwon, S.-H.; Lee, G.; Motoyama, K.; Kim, M. W.; Lin, M.; Niidome, T.; Choi, J. H.; Lee, R. pH-sensitive multi-drug liposomes targeting folate receptor β for efficient treatment of non-small cell lung cancer. *J. Controlled Release* **2021**, *330*, 1–14.
- (32) Hao, Y.; Liu, Y.; Wu, Y.; Tao, N.; Lou, D.; Li, J.; Sun, X.; Liu, Y.-N. A Robust Hybrid Nanozyme@hydrogel Platform as a Biomimetic Cascade Bioreactor for Combination Antitumor Therapy. *Biomater. Sci.* **2020**, *8*, 1830–1839.
- (33) Appidi, T.; Pemmaraju, D. B.; Khan, R. A.; Alvi, S. B.; Srivastava, R.; Pal, M.; Khan, N.; Rengan, A. K. Light-Triggered Selective ROS-Dependent Autophagy by Bioactive Nanoliposomes for Efficient Cancer Theranostics. *Nanoscale* **2020**, *12*, 2028–2039.
- (34) Yang, F.; Shi, K.; Jia, Y.; Hao, Y.; Peng, J.; Yuan, L.; Chen, Y.; Pan, M.; Qian, Z. A biodegradable thermosensitive hydrogel vaccine for cancer immunotherapy. *Appl. Mater. Today* **2020**, *19*, 100608.
- (35) Chen, Z.; Liu, L.; Liang, R.; Luo, Z.; He, H.; Wu, Z.; Tian, H.; Zheng, M.; Ma, Y.; Cai, L. Bioinspired Hybrid Protein Oxygen Nanocarrier Amplified Photodynamic Therapy for Eliciting Anti-Tumor Immunity and Abscopal Effect. *ACS Nano* **2018**, *12*, 8633–8645.
- (36) Fu, J.; Wu, B.; Wei, M.; Huang, Y.; Zhou, Y.; Zhang, Q.; Du, L. Prussian Blue Nanosphere-Embedded in Situ Hydrogel for Photothermal Therapy by Peritumoral Administration. *Acta Pharm. Sin. B* **2019**, *9*, 604–614.
- (37) Wakamatsu, K.; Ito, S. Advanced Chemical Methods in Melanin Determination. *Pigm. Cell Res.* **2002**, *15*, 174–183.
- (38) Li, Z.; Chen, Y.; Yang, Y.; Yu, Y.; Zhang, Y.; Zhu, D.; Yu, X.; Ouyang, X.; Xie, Z.; Zhao, Y.; Li, L. Recent Advances in Nanomaterials-Based Chemo-Photothermal Combination Therapy for Improving Cancer Treatment. *Front. Bioeng. Biotechnol.* **2019**, *7*, 1–19.
- (39) Tobitani, A.; Ross-Murphy, S. B. Heat-Induced Gelation of Globular Proteins. 1. Model for the Effects of Time and Temperature on the Gelation Time of BSA Gels. *Macromolecules* **1997**, *30*, 4845.
- (40) Baler, K.; Michael, R.; Szeleifer, I.; Ameer, G. A. Albumin Hydrogels Formed by Electrostatically Triggered Self-Assembly and Their Drug Delivery Capability. *Biomacromolecules* **2014**, *15*, 3625.
- (41) Jain, T. K.; Foy, S. P.; Erokku, B.; Dimitrijevic, S.; Flask, C. A.; Labhasetwar, V. Magnetic Resonance Imaging of Multifunctional Pluronic Stabilized Iron-Oxide Nanoparticles in Tumor-Bearing Mice. *Biomaterials* **2009**, *30*, 6748–6756.
- (42) Kharazmi, A.; Faraji, N.; Mat Hussin, R.; Saion, E.; Yunus, W. M. M.; Behzad, K. Structural, Optical, Opto-Thermal and Thermal Properties of ZnS-PVA Nanofluids Synthesized through a Radiolytic Approach. *Beilstein J. Nanotechnol.* **2015**, *6*, 529–536.
- (43) Neacsu, M. V.; Matei, I.; Micutz, M.; Staicu, T.; Precupas, A.; Popa, V. T.; Salifoglou, A.; Ionita, G. Interaction between Albumin and Pluronic F127 Block Copolymer Revealed by Global and Local Physicochemical Profiling. *J. Phys. Chem. B* **2016**, *120*, 4258–4267.
- (44) Xiong, J.; Yan, J.; Li, C.; Wang, X.; Wang, L.; Pan, D.; Xu, Y.; Wang, F.; Li, X.; Wu, Q.; Liu, J.; Liu, Y.; Liu, Q.; Zhou, Y.; Yang, M. Injectable Liquid Metal Nanoflake Hydrogel as a Local Therapeutic for Enhanced Postsurgical Suppression of Tumor Recurrence. *Chem. Eng. J.* **2021**, *416*, 129092.
- (45) Zhong, Y.; Wang, C.; Cheng, L.; Meng, F.; Zhong, Z.; Liu, Z. Gold Nanorod-Cored Biodegradable Micelles as a Robust and Remotely Controllable Doxorubicin Release System for Potent Inhibition of Drug-Sensitive and -Resistant Cancer Cells. *Biomacromolecules* **2013**, *14*, 2411–2419.
- (46) Liao, J.; Li, W.; Peng, J.; Yang, Q.; Li, H.; Wei, Y.; Zhang, X.; Qian, Z. Combined Cancer Photothermal-Chemotherapy Based on Doxorubicin/Gold Nanorod-Loaded Polymersomes. *Theranostics* **2015**, *5*, 345–356.
- (47) Shao, J.; Xie, H.; Huang, H.; Li, Z.; Sun, Z.; Xu, Y.; Xiao, Q.; Yu, X.-F.; Zhao, Y.; Zhang, H.; Wang, H.; Chu, P. K. Biodegradable Black Phosphorus-Based Nanospheres for in Vivo Photothermal Cancer Therapy. *Nat. Commun.* **2016**, *7*, 12967.

- (48) Liu, Y.; Yang, M.; Luo, J.; Zhou, H. Radiotherapy Targeting Cancer Stem Cells “Awakens” Them to Induce Tumour Relapse and Metastasis in Oral Cancer. *Int. J. Oral Sci.* **2020**, *12*, 19.
- (49) Shao, J.; Ruan, C.; Xie, H.; Li, Z.; Wang, H.; Chu, P. K.; Yu, X.-F. Black-Phosphorus-Incorporated Hydrogel as a Sprayable and Biodegradable Photothermal Platform for Postsurgical Treatment of Cancer. *Adv. Sci.* **2018**, *5*, 1700848.
- (50) Esmatabadi, M. J. D.; Bakhshinejad, B.; Motlagh, F. M.; Babashah, S.; Sadeghizadeh, M. Therapeutic Resistance and Cancer Recurrence Mechanisms: Unfolding the Story of Tumour Coming Back. *J. Biosci.* **2016**, *41*, 497–506.
- (51) Rohani, N.; Hao, L.; Alexis, M. S.; Joughin, B. A.; Krismer, K.; Moufarrej, M. N.; Soltis, A. R.; Lauffenburger, D. A.; Yaffe, M. B.; Burge, C. B.; Bhatia, S. N.; Gertler, F. B. Acidification of Tumor at Stromal Boundaries Drives Transcriptome Alterations Associated with Aggressive Phenotypes. *Cancer Res.* **2019**, *79*, 1952–1966.
- (52) Jain, R. K.; Martin, J. D.; Stylianopoulos, T. The Role of Mechanical Forces in Tumor Growth and Therapy. *Annu. Rev. Biomed. Eng.* **2014**, *16*, 321–346.
- (53) Alvi, S. B.; Appidi, T.; Deepak, B. P.; Rajalakshmi, P. S.; Minhas, G.; Singh, S. P.; Begum, A.; Bantal, V.; Srivastava, R.; Khan, N.; Rengan, A. K. The “nano to micro” transition of hydrophobic curcumin crystals leading to in situ adjuvant depots for Au-liposome nanoparticle mediated enhanced photothermal therapy. *Biomater. Sci.* **2019**, *7*, 3866–3875.
- (54) Mebius, R. E.; Kraal, G. Structure and Function of the Spleen. *Nat. Rev. Immunol.* **2005**, *5*, 606–616.
- (55) P.S., R.; Alvi, S. B.; Begum, N.; Veeresh, B.; Rengan, A. K. Self-Assembled Fluorosome-Polydopamine Complex for Efficient Tumor Targeting and Commingled Photodynamic/Photothermal Therapy of Triple-Negative Breast Cancer. *Biomacromolecules* **2021**, *22*, 3926.
- (56) Kano, A. Tumor Cell Secretion of Soluble Factor(s) for Specific Immunosuppression. *Sci. Rep.* **2015**, *5*, 8913.
- (57) Golombek, S. K.; May, J.-N.; Theek, B.; Appold, L.; Drude, N.; Kiessling, F.; Lammers, T. Tumor Targeting via EPR: Strategies to Enhance Patient Responses. *Adv. Drug Deliv. Rev.* **2018**, *130*, 17–38.
- (58) Sun, H.; Su, J.; Meng, Q.; Yin, Q.; Chen, L.; Gu, W.; Zhang, Z.; Yu, H.; Zhang, P.; Wang, S.; Li, Y. Cancer Cell Membrane-Coated Gold Nanocages with Hyperthermia-Triggered Drug Release and Homotypic Target Inhibit Growth and Metastasis of Breast Cancer. *Adv. Funct. Mater.* **2017**, *27*, 1604300.
- (59) Liu, X.; Lin, P.; Perrett, I.; Lin, J.; Liao, Y.-P.; Chang, C. H.; Jiang, J.; Wu, N.; Donahue, T.; Wainberg, Z.; Nel, A. E.; Meng, H. Tumor-Penetrating Peptide Enhances Transcytosis of Silicasome-Based Chemotherapy for Pancreatic Cancer. *J. Clin. Invest.* **2017**, *127*, 2007–2018.
- (60) Su, J.; Sun, H.; Meng, Q.; Yin, Q.; Tang, S.; Zhang, P.; Chen, Y.; Zhang, Z.; Yu, H.; Li, Y. Long Circulation Red-Blood-Cell-Mimetic Nanoparticles with Peptide-Enhanced Tumor Penetration for Simultaneously Inhibiting Growth and Lung Metastasis of Breast Cancer. *Adv. Funct. Mater.* **2016**, *26*, 1243.
- (61) Pak, B. J.; Lee, J.; Thai, B. L.; Fuchs, S. Y.; Shaked, Y.; Ronai, Z. e.; Kerbel, R. S.; Ben-David, Y. Radiation Resistance of Human Melanoma Analysed by Retroviral Insertional Mutagenesis Reveals a Possible Role for Dopachrome Tautomerase. *Oncogene* **2004**, *23*, 30–38.
- (62) Brożyna, A. A.; VanMiddlesworth, L.; Slominski, A. T. Inhibition of Melanogenesis as a Radiation Sensitizer for Melanoma Therapy. *Int. J. Cancer* **2008**, *123*, 1448–1456.



(12) **United States Patent**
Syed et al.

(10) Patent No.: US 11,938,186 B2
(45) Date of Patent: Mar. 26, 2024



US 11,938,186 B2

(54) **THERMOSENSITIVE HYDROGEL FOR
CANCER THERAPEUTICS AND METHODS
OF PREPARATION THEREOF**

(71) Applicant: **INDIAN INSTITUTE OF
TECHNOLOGY HYDERABAD,**
Telangana (IN)

(72) Inventors: **Basavaraddi Alvi Syed, Sangareddy**
(IN); **Rajalakshmi P. S., Sangareddy**
(IN); **Araavind Kumar Rengan,**
Sangareddy (IN)

(73) Assignee: **Indian Institute of Technology**
Hyderabad, Telangana (IN)

(*) Notice: Subject to any disclaimer, the term of this
patent is extended or adjusted under 35
U.S.C. 154(b) by 258 days.

(21) Appl. No.: 17/325,290

(22) Filed: May 20, 2021

(65) **Prior Publication Data**
US 2021/0303780 A1 Dec. 23, 2021

(58) **Field of Classification Search**

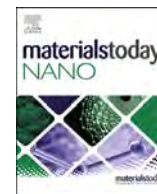
Name:

See application file for complete search history

(56) **References Cited**

PUBLICATIONS

Giuliano et al (Drug-Loaded Biocompatible Nanocarriers Embed-
ded in Poxosamer 407 Hydrogels as Therapeutic Formulations,
Medicine 2019, 6, 7, p. 1-20) (Year: 2019).
Giuliano et al (Mutual Applications of Poxosamer 407-Based
Hydrogels: An Overview, Pharmaceutics 2018, 10, 159, p. 1-26;
herein after "Giuliano"), (Year: 2018).
Benea et al (Temperature Responsive Gels Based on Pluronic F127
and Poly(vinyl alcohol), Int. J.ug. Chem. Res. 2011, 50, 4195-4206
(Year: 2011).
And Kamtongrak et al (Lamellar phase behavior and molecular
interaction of a thermoresponsive poxosamer and crosslinked poly
(vinyl alcohol) hydrogel, Materials Today Communications, <https://doi.org/10.1016/j.matcom.2019.100542>, p. 1-13) (Year: 2019).
Drekon et al (The golden age: gold nanoparticles for biomedicine,
Chem Soc Rev Apr. 3, 2012; 41(7): 2740-2779) (Year: 2012).
Liu et al (Codelivery of Doxorubicin and Paclitaxel by Cross-
Linked Multilamellar Liposome Enables Synergistic Antitumor
Activity Mol. Pharmaceutics 2014, 11, 1651-1661) (Year: 2014).
* cited by examiner



Bioinspired gold coated phage nanosomes for anti-microbial and anti-cancer theranostics

D.N. Yadav¹, S.A. Sankaranarayanan¹, A.M. Thanekar, A.K. Rengan*

Department of Biomedical Engineering, Indian Institute of Technology Hyderabad, Kandi, 502284, India

ARTICLE INFO

Article history:

Received 20 November 2022

Received in revised form

9 April 2023

Accepted 2 May 2023

Available online 6 May 2023

Keywords:

Bacteriophage

Gold nanosomes

Photothermal therapy

Mitoxantrone

Microbial infections

Cancer

ABSTRACT

We report a unique bioinspired phage nanosome as a biological template for tuning the NIR absorbance of gold nanoparticles ($\Phi_{NS}Au$) coated on its surface. Spectroscopical analysis revealed that the presence of phage significantly enhances the optical properties of encapsulated dyes, rendering them excellent imaging agents. *In vitro*, studies showed the excellent photothermal transduction efficacy of the developed $\Phi_{NS}Au$ in combination with a chemotherapeutic drug, Mitoxantrone ($\Phi_{NS}AuM$). $\Phi_{NS}AuM$ mediated photothermal therapy (PTT) using a 690 nm laser exhibited excellent anti-microbial activity against *E. coli* and *C. albicans*. *In vitro* and *in ovo* studies using zebrafish embryos revealed excellent biocompatibility, no/minimal cardiotoxicity, and enhanced internalization of phage-based nanosomes when compared with respective liposomal controls. When tested against 4T1 cell lines, the synthesized $\Phi_{NS}AuM$ exhibited significant synergistic anti-cancer activity with enhanced ROS generation and subsequent mitochondrial damage. The blood vessel rupturing potential of $\Phi_{NS}AuM$ mediated PTT has been demonstrated using an *in ovo* chick chorioallantoic membrane (CAM) assay, thus proving it as a potential photothermal agent. Overall, the developed phage-based nanosomes facilitated enhanced PTT efficacy, thereby showing an encouraging potential for anti-microbial and anti-cancer theranostics.

© 2023 Elsevier Ltd. All rights reserved.

1. Introduction

Nanomaterials have drawn the attention of researchers for their versatility in biomedical applications, particularly in disease theranostics [1]. In the recent past, a strong link between cancer and microbial infections has been established [2,3]. Due to the compromised immune system, occasional neutropenia (an adverse effect of prolonged chemotherapy), and disruption of the normal anatomical barriers in superficial tumors (owing to surgical resection or radiation damage), microbial infections are the most complicated consequences in cancer patients [4–8]. It has been reported that *E. coli* is the primary cause of bacteremia in cancer patients [9]. Along similar lines, cancer patients are also prone to fungal infections, leading to aspergillosis and *Candida* sepsis [10]. Additionally, certain microbial infections also pose cancer-causing threats [11]. For instance, *H. pylori* is a well-known factor causing gastrointestinal cancer [6,11,12]. Under certain circumstances, the commensals in the gut become opportunistic pathogens,

culminating in increased cancer risks [6,12]. Recently, it has been reported that patients with candidiasis are prone to increased cancer risks [10,13,14]. Hence, a theranostic strategy capable of eliminating microbial infections and simultaneously killing tumor cells is warranted.

NIR laser driven phototherapies have emerged as a non-invasive, affordable alternative to existing radiation therapy due to the penetration depth offered by the NIR window. Photothermal therapy (PTT) employs plasmonic nanomaterials that convert the absorbed incident NIR light into heat, resulting in the localized ablation of cancer cells [15–17]. Recently, the spatial control offered by PTT and its non-specific nature has been utilized to extend the application of PTT in treating superficial microbial infections [18,19]. Generally, nanomaterials of metals such as gold, copper, etc., semiconductor dots, and NIR dyes are used in PTT. However, they are often associated with toxicity, poor biodegradability, and pharmacokinetic/pharmacodynamic profile [20]. Real-time monitoring of treatment efficacy plays a major role in improving the therapeutic index of any modality. This is achieved by tracking the nanoparticle accumulation and biodistribution and assessing the tumor size and morphology through various optical and fluorescence-based imaging techniques [20]. Several contrast

* Corresponding author.

E-mail address: aravind@bme.iith.ac.in (A.K. Rengan).

¹ These authors contributed equally.

agents (made up of iron, gold, gadolinium, etc) have been developed for CT, MRI, or PET-based imaging [21,22]. Moreover, besides being excellent photosensitizers, NIR dyes (such as IR780, IR806, ICG, etc.) also aid in fluorescence-based imaging [20]. However, their applications are limited by the complex conjugation process, low photostability, and high dose requirement for a readable fluorescence signal under physiological conditions [20]. Hence, a single nanoentity tailor-made to kill tumor cells with real-time monitoring of its efficacy is in high demand. Moreover, nanotechnology offers the additional advantage of integrating multiple modalities within a single nanoentity for a synergistic effect (chemo-photothermal therapy, photothermal-immunotherapy, etc.) [23–25].

The use of surface plasmon resonance of gold nanoparticles in PTT dates back decades to the development of silica-gold-based nanostructures. This led to the development of various biodegradable templates (cores) for tuning the NIR absorbance of gold coated over their surfaces. However, they are limited due to their poor biodegradability, expensive cost, and batch-to-batch variation. Hence, there is a demand for exploring unique biodegradable template materials to overcome the existing limitations. Cell primitives formed from biological systems, such as bacteria, bacteriophages, cell membranes, etc., belong to a new generation of bio-inspired/living therapeutics to overcome the limitations of existing synthetic nanomaterials [26,27]. Bacteriophages, also called phages (Φ), have drawn considerable attention as a protein-based nanoplatform. [28,29] Given their unique shape and stability at higher temperatures, a wide range of pH levels, and resistance to degrading enzymes such as DNases and RNases, these phages offer additional advantages over conventional synthetic nanomaterials [27]. Moreover, the nano-size of the phages could be easily tuned to overcome the biological barriers, aid in site-specific delivery, and escape immune surveillance [24,30–32].

In this study, we have developed bioinspired phage based nanosomes (Φ_{NS}) and tuned them into being photothermally active via gold coating over their surface ($\Phi_{NS}Au$). In addition to its potential anti-cancer activity, mitoxantrone (MTX) has also been well studied for its antimicrobial activity. For a synergistic PTT, the Φ_{NS} were loaded with MTX ($\Phi_{NS}AuM$) and subsequently coated with gold for PTT applications. The developed nanosomes were characterized by their size, shape, PTT transduction efficiency, and photothermal stability. The as-synthesized $\Phi_{NS}AuM$ demonstrated potential anti-bacterial activity against *E.coli*, when irradiated with an NIR laser of 690 nm, confirmed by colony formation assay. The $\Phi_{NS}AuM$ also showed excellent PTT-mediated antifungal activity against *Candida.albicans*, evaluated by spot assay, calcofluor white staining (CWS), and FESEM analysis. The phage nanosomes were loaded with tracker dye, Nile Red (NR) prior to gold coating to evaluate the cellular internalization of $\Phi_{NS}Au$. The biocompatibility, biodistribution, and effect of $\Phi_{NS}Au$ on cardiac rhythm were evaluated using *ovo* zebrafish embryo models. The photothermal application of $\Phi_{NS}AuM$ was tested on 4T1 breast cancer cell lines by MTT assay. Furthermore, NIR laser-mediated ROS generation and mitochondrial damage were evaluated in 4T1 cell lines in the presence of $\Phi_{NS}AuM$. We further assessed the effect of $\Phi_{NS}AuM$ mediated PTT on neo-blood vessels using a chick embryo model using a chick chorioallantoic membrane (CAM) assay. Overall, the synthesized $\Phi_{NS}AuM$ displayed excellent photothermal properties against *E.coli*, *C.albicans*, and 4T1 breast cancer cells (as depicted in schematic Fig. 1), thus paving the way for the development of novel therapeutics based on living materials.

2. Materials and methods

2.1. Chemicals

Tetrachloroauric acid trihydrate ($HAuCl_4 \cdot 3H_2O$), ascorbic acid, and fluorescein diacetate were purchased from Sigma Aldrich Pvt. Ltd., India. Mitoxantrone was purchased from TCI Chemicals Pvt. Ltd. Egg Phosphatidyl Choline (Egg PC) was purchased from SRL Chemicals, India. Dulbecco's modified Eagle medium (DMEM), fetal bovine serum (FBS), Pen-strep solution, phosphate-buffered saline (PBS), Thiazolyl Blue Tetrazolium Bromide (MTT), and Trypsin EDTA solution were purchased from Himedia Laboratories, Mumbai (India). Propidium iodide and (4',6-diamidino-2-phenylindole) DAPI were purchased from Sigma. All other reagents used were of analytical grade.

2.2. Plaque formation assay or quantifying phage

Plaque formation assays were done using the agar layer technique. Phage particles were initially diluted in a suspension buffer, allowing adsorption onto the surface of *E.coli* C600 bacterial cells incubated at 37 °C. In two eppendorfs, 100 μ L of *E.coli* culture (1.0 OD) was added with 100 μ L of 10^{-5} and 10^{-7} dilutions of phage in suspension buffer and incubated for 20 min at 37 °C. Further, 3 mL of melted soft agar (1/2% agar) was added to the above culture containing *E.coli* and phage. The soft agar-containing culture was poured onto the LB agar plate containing 5 mM $MgSO_4$ and rotated to spread the culture all over the plate. The plates were then incubated at 37 °C for 24 h to evaluate plaque formation [33].

2.3. Synthesis of phage nanosomes (Φ_{NS})

Φ_{NS} were synthesized by the ethanol injection method, as previously reported. Briefly, 20 mg of Egg PC was dissolved in ethanol and added dropwise to Milli Q (MQ) water containing phage particles (3.95×10^{10} PFU/mL) preheated at 65 °C under stirring at 1000 rpm. The mixture was sonicated for 2 min after 15–20 min of vigorous stirring. For MTX-loaded nanosomes ($\Phi_{NS}M$), a similar procedure was followed, wherein Egg PC and MTX were dissolved in ethanol at a ratio of 20:0.5 [34].

2.4. Preparation of gold-coated phage nanosomes ($\Phi_{NS}Au$)

The nanosomes were coated with gold on their surface, as reported earlier, with minor modifications. Briefly, 100 μ L Φ_{NS} & $\Phi_{NS}M$ (2 mg/mL) were mixed with $HAuCl_4$ (2 mM; 200 μ L). Ascorbic acid (20 mM; 50 μ L) was then added to the mixture by vigorous pipetting. A rapid color change was observed as the solution turned dark blue, indicating the formation of $\Phi_{NS}Au/\Phi_{NS}AuM$. The prepared Φ_{NS} were further characterized for particle size and morphology [17].

2.5. Characterization of phage nanosomes

The synthesized nanosomes were characterized for their UV absorbance using a UV–vis spectrophotometer (Shimadzu UV-1800, Japan). The hydrodynamic diameter of the as-synthesized nanosomes pre and post-laser irradiation were evaluated using the dynamic light scattering technique (Particle Sizing Systems, Inc., Santa Barbara, California, USA). The morphology and size of nanosomes were visualized using a scanning electron microscope, FE-SEM (Carl Zeiss atomic microscope, Supra40, Germany), and a

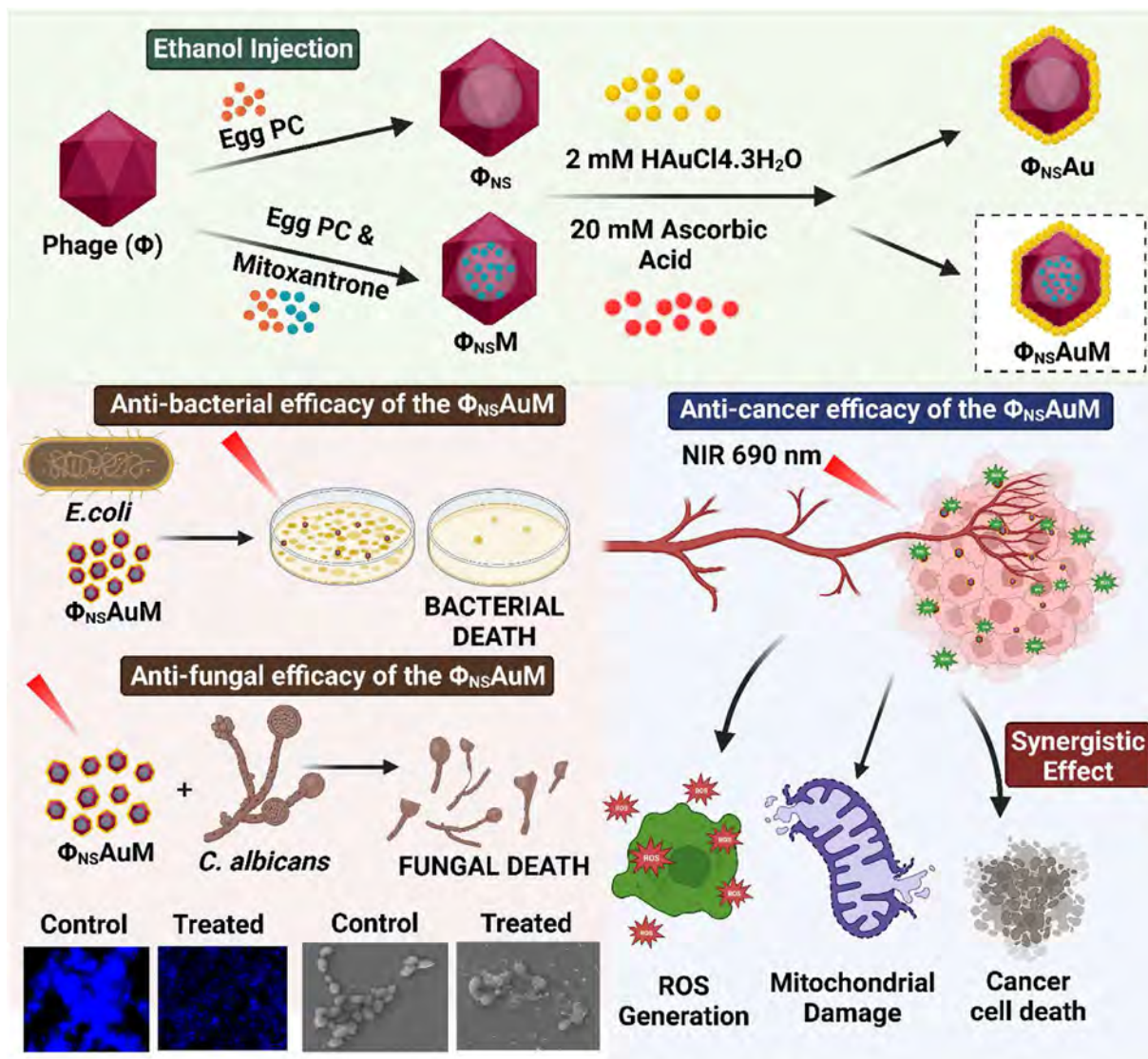


Fig. 1. Schematic depiction of the synthesis & applications of gold coated MTX phage nanosomes ($\Phi_{NS}AuM$).

transmission electron microscope (FE-TEM, JEM-2200, JEOL Inc., USA; 200 KV).

2.6. PTT transduction efficacy of phage nanosomes

The photothermal transduction efficiency of $\Phi_{NS}Au$, and $\Phi_{NS}AuM$, upon irradiation with a 690 nm NIR laser at a power of 650 mW (Shanghai Inter-Diff Optoelectronics Technology Ltd., Shanghai, China) was recorded using an infrared thermal imaging camera (Chauvin Arnoux, CA 1950 DiaCam IR Camera IP 54, Paris, France). MQ and standard gold nanoparticles were used as controls. The temperature rise vs time was plotted for all the tested samples. Photothermal stability was evaluated by repeated laser irradiation of the samples for five cycles. The thermal images were acquired at the end of 10 min of irradiation for five cycles.

2.7. Anti-microbial efficacy of $\Phi_{NS}AuM$

2.7.1. NIR light-mediated anti-bacterial efficacy of the $\Phi_{NS}AuM$

The NIR light-mediated anti-bacterial efficacy studies of Au, LAu, $\Phi_{NS}Au$, and $\Phi_{NS}AuM$ were performed using an inoculum of *E. coli*

culture as per the standard institute protocols. Briefly, *E. coli* inoculum of 2×10^8 CFU/mL was prepared, followed by treatment with 100 μ g/mL of Au, LAu, $\Phi_{NS}Au$, and $\Phi_{NS}AuM$ incubated for 2 h in two 96-well plates. One plate was further incubated without treatment (-NIR group), and the other plate was exposed to 690 nm light using a laser (+NIR) for 10 min and incubated at 37 °C for 24 h. After the incubation period, a colony formation assay was performed. Briefly, 100 μ L from the 8-fold serial dilutions of the inoculum from the treated 96-well plates was spread onto MH Agar plates, and untreated controls were also plated using the same procedure and incubated for 16 h at 37 °C. The difference in the number of colonies was evaluated after the incubation period.

2.7.2. NIR light-mediated anti-fungal efficacy of the $\Phi_{NS}AuM$

The NIR light-mediated anti-fungal efficacy studies of $\Phi_{NS}AuM$ were performed using an inoculum of *C. albicans* culture as per the standard institute protocols. Briefly, a *C. albicans* inoculum of 2×10^3 CFU/mL was prepared, followed by treatment with 100 μ g/mL of Au, LAu, $\Phi_{NS}Au$, and $\Phi_{NS}AuM$ incubated for 2 h in two 96-well plates. One plate was further incubated without treatment (-NIR group), and the other plate was exposed to 690 nm light using a

laser for 10 min (+ NIR group) and incubated at 37 °C for 48 h. After the incubation period, a spot assay was performed. Briefly, 1 mL of 7-fold serial dilutions of the inoculum (10^0 , 10^{-1} , 10^{-2} , 10^{-3} , 10^{-4} , 10^{-5} and 10^{-6}) from the treated 96-well plates was spotted on SD agar plates, and untreated controls were also plated using the same procedure. The difference in colony formation and spot size was estimated after 24 h of incubation at 37 °C. Also, to understand the morphological difference upon treatment, both the control and culture were treated with Φ_{NSAuM} and NIR laser irradiation for 10 min. 10 μ L of the culture was dropped onto a clean glass slide and immediately stained with an equal amount of calcofluor white stain and 10% potassium hydroxide (KOH). Subsequently, the sample was mounted using a clean coverslip, and excess stains were blotted and allowed to dry for 2 min. The samples were then observed under UV light using a fluorescent cell imager (Zoe, BioRad, USA) [35,36].

2.7.3. FE-SEM analysis of PTT-mediated killing of *C. albicans*

To evaluate the structural and morphological damage in *C. albicans* upon treatment with Φ_{NSAuM} with NIR light exposure, an FE-SEM (Carl Zeiss atomic microscope, Supra40 Germany) analysis was performed. The fungal culture was allowed to attach to a Poly-L-Lysine coated coverslip. Upon attachment, cells were incubated with Φ_{NSAuM} for 2 h followed by exposure to a 690 nm laser irradiation for 10 min. The cells were fixed with 2% glutaraldehyde for 2 h, followed by sequential dehydration using 30%, 50%, 70%, 90%, and 100% ethanol. The samples were allowed to dry overnight and sputter-coated for 10 s with gold before FE-SEM analysis [37].

2.8. In vitro studies

2.8.1. Biocompatibility of Φ_{NSAu}

L929 cells were used to evaluate the biocompatibility of the synthesized Φ_{NSAu} . Briefly, 1×10^4 cells/well were seeded. Upon incubation for 24 h, the attached cells were treated with varying concentrations of Φ_{NSAu} for 24 h. The cell viability was then quantified using MTT assay after 24 h of treatment [38].

2.8.2. Cellular internalization of Φ_{NSAu}

To evaluate the cellular internalization of Φ_{NSAu} , 4T1 cells were seeded at a density of 20×10^4 cells/well on a coverslip in a 24-well plate. After 24 h of incubation, the cells were treated with LAuM and Φ_{NSAuM} for 5 h. Subsequently, the cells were washed with 1X PBS and fixed with 4% paraformaldehyde (PFA). The cells were stained with DAPI and imaged under a live cell imager. (Zoe, BioRad, USA). To evaluate the mitochondrial localization of the developed Φ_{NSAuM} , a similar methodology was adopted, wherein the cells were stained with 10 μ M of MitoGreen post-fixation with 4% PFA for 30 min. The cells were then imaged under the live cell imager.

2.8.3. Anti-cancer efficacy of Φ_{NSAuM}

The *in vitro* anti-cancer efficacy of the synthesized Φ_{NSAuM} was evaluated using 4T1 cell lines. The photothermal killing of 4T1 cells using Φ_{NSAuM} and the synergistic effect in combination with MTX were initially assessed using the MTT assay. Briefly, 1×10^4 4T1 cells/well were seeded in a 96-well plate, and upon attachment, the cells were treated with LAu, Φ_{NSAu} , and Φ_{NSAuM} . The cells were then irradiated with a 690 nm laser for 10 min 24 h post-treatment, the cell viability was quantified [38].

The ROS generation upon laser irradiation in the presence of Φ_{NSAu} and Φ_{NSAuM} was evaluated using the DCFDA assay. Briefly, 1×10^4 cells/well were seeded in a 96-well plate, and upon attachment, the cells were treated with LAu, Φ_{NSAu} , and Φ_{NSAuM} . 10 μ M of DCFDA was added before irradiation with a 690 nm laser

for 10 min. The cells were then visualized under a fluorescence microscope.

The effect of the Φ_{NSAu} and Φ_{NSAuM} mediated PTT on the mitochondrial membrane potential was evaluated using JC1 staining. Briefly, the cells upon treatment with LAu, Φ_{NSAu} , and Φ_{NSAuM} were irradiated using a 690 nm laser for 10 min. After 6 h post-treatment, the cells were stained with 10 μ g/mL of JC1 stain for 30 min. The excitation and emission of the J aggregate (Ex: 535 nm and Em: 595 nm) and J monomer (Ex: 485 nm and Em: 535 nm) were recorded using a microplate reader, and the images were captured using a live cell imager. The red-green fluorescence was further plotted to depict the mitochondrial damage [39].

2.8.4. Evaluation of uptake and PTT efficacy in 3D spheroids

To evaluate the uptake of nanosomes and the photothermal efficacy, 3D spheroids of 4T1 cells (3000 cells/drop) were developed using the hanging-drop method. At day 5 of spheroid formation, the spheroids were treated with LAuM and Φ_{NSAuM} for 5 h. Post-treatment, the spheroids were imaged under a live cell imager (Zoe, BioRad, USA). For evaluation of PTT efficacy, the spheroids at day 5 were treated with Φ_{NSAuM} and then irradiated with 690 nm for 10 min. Upon 24 h post-treatment, the spheroids were added with 1 μ L of FDA (5 mg/mL) and PI (1 mg/mL) each to assess the viability of the cells.

2.9. In ovo PTT efficacy of Φ_{NSAu} (CAM assay)

The *in ovo* CAM assay was conducted using fertilized hen eggs, which were obtained from the local Kandi village in Hyderabad. The eggs were incubated horizontally under shaking conditions (HHD-24S digital egg incubator, made in India) at 37 °C with 70% humidity for about 4 days. After the incubation period, the formation of blood vessels was visualized using a digital microscope and hand camera. Under sterile conditions, the eggshell was opened on the snub side with the help of forceps and a needle, and about 2–3 mL of albumin content was removed from the egg using a syringe. The hole was further sealed with a thin parafilm. On the opposite end, where the blood vessels were visible, a small incision was made with the help of needles and forceps. The NIR light-mediated blood vessel rupturing effect of Au, LAu, Φ_{NSAu} , and Φ_{NSAuM} was evaluated on these eggs. About 100 μ g/mL of each particle was injected into the blood vessels, incubated for 2 h, and then exposed to a 690 nm laser for 10 min. Post-treatment, the blood vessels were observed and captured using a digital microscope and hand camera to detect their rupturing properties [38,40].

2.10. In ovo biocompatibility uptake in zebrafish embryo

2.10.1. Evaluation of survivability, biodistribution, and cardiac rhythm

For survivability analysis, 20 embryos were taken per well per group in 2 mL of 1X E3 (1.46 g NaCl, 0.063 g KCl, 0.243 g $\text{CaCl}_2 \cdot 2\text{H}_2\text{O}$, and 0.407 g $\text{MgSO}_4 \cdot 7\text{H}_2\text{O}$ in 1 L of DI water with pH adjusted to 7.2 using 0.1 N NaOH). The embryos were treated with LAu and Φ_{NSAu} and the embryos were observed up to 4 days post fertilization. The number of viable and dead embryos was recorded using microscopic analysis. At 4 dpf, the heartbeat was captured under the microscope to evaluate the effect of Φ_{NSAu} on the cardiac rhythm. The cardiac rhythm analysis was performed as per previous reports to obtain the heartbeat per minute.

For biodistribution analysis, nanosomes loaded with NR were used. Briefly, embryos were treated with free NR and NR-loaded LAu and Φ_{NSAu} on days 1 and 3 dpf. The internalization of the nanosomes was imaged under the fluorescence microscope 24 h post-treatment.

3. Results and discussion

3.1. Plaque formation assay

A plaque formation assay was performed to quantify the phage and its plaque formation ability. As shown in [Supplementary Fig. S1 A&B](#), it was observed that 100 μL of *E.coli* overnight grown culture and 10^{-5} dilution of phage in suspension buffer gave 8.9×10^8 PFU/mL and the same with 10^{-7} dilution of phage in suspension buffer gave 7.9×10^7 PFU/mL. The cultured phage particles were also characterized using SEM ([Fig. 2A](#)), and the modified phage nanosomes were characterized using TEM ([Fig. 2B](#)).

3.2. Synthesis and characterization of Φ_{NSAu}

Phage nanosomes were tuned into being photothermally active by coating their surface with gold and using *in situ* reduction of HAuCl_4 with ascorbic acid. Upon the addition of ascorbic acid, a

rapid change in the color of the solution from yellow to dark blue was observed, confirming the presence of gold-coated Φ_{NS} . The UV–Vis absorbance spectrum showed a broad peak in the NIR region from 670 nm to 730 nm ([Fig. 2C](#)) when compared to gold-coated liposomes, which exhibited absorbance at 600 nm. The absorbance was 547 nm when MQ was used as a template, showing the formation of gold nanoparticles. The hydrodynamic diameter of the synthesized Φ_{NSAu} was found to be 197 nm ([Fig. 2D](#)), concordant with SEM ([Fig. 2E](#)) and TEM ([Fig. 2F](#)) imaging, revealing the size of the Φ_{NSAu} in the range of 100–120 nm. The photothermal transduction efficacy of the synthesized Φ_{NSAu} was evaluated by recording the rise in temperature upon irradiation with a 690 nm laser for 10 min. It was found that the temperature rose up to $51.3 \pm 1^\circ\text{C}$ ([Fig. 2G](#) and [H](#)), showing the potential of the synthesized Φ_{NSAu} as an excellent photothermal agent compared with control Lipos Gold (LAu) nanosomes ([Supplementary Fig. S2](#)). [Table S1](#) summarizes the hydrodynamic diameters of the template nanosomes and gold-coated nanosomes.

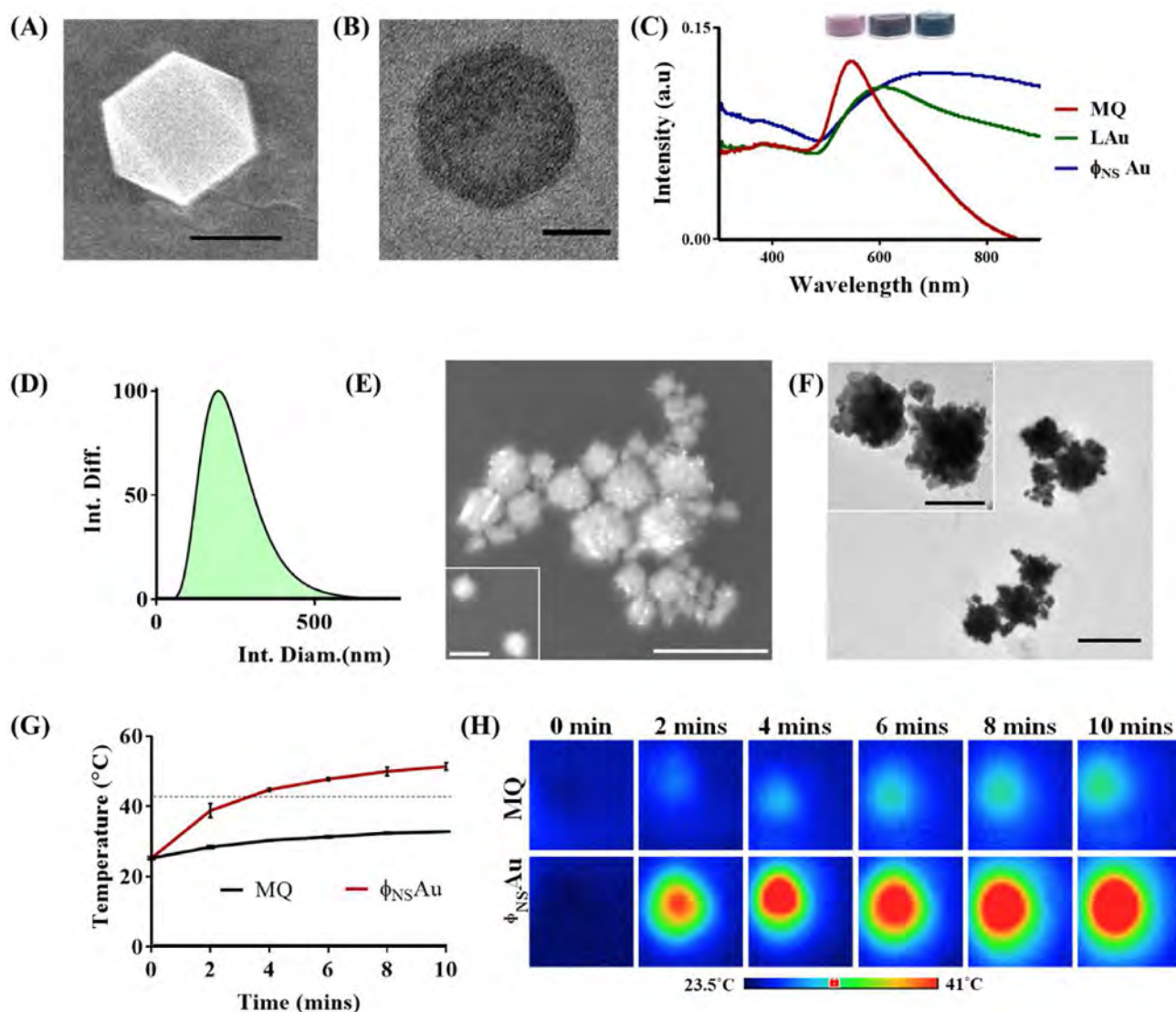


Fig. 2. Synthesis & Characterization of gold coated phage nanosomes (Φ_{NSAu}). (A) & (B) FESEM and TEM imaging of phage and modified phage nanosomes respectively (Scale bar represents 0.5 μm and 50 nm respectively). (C) UV–Vis absorbance spectra (Inset: Photographs of synthesized nanoparticles; 1-MQ, 2- LAu, 3- Φ_{NSAu}), (D) Hydrodynamic diameter, (E) FESEM analysis, (F) TEM analysis, (G) Temperature vs time plot & (H) Thermal images of Φ_{NSAu} . (Scale bar in (E) represents 500 nm and inset 200 nm; Scale bar in (F) represents 200 nm and inset 100 nm).

3.3. Drug loading

For a synergistic PTT effect, the phage nanosomes were loaded with a known chemotherapeutic drug, MTX. Recently, MTX has also been reported for its potential anti-microbial properties. Briefly, egg PC and MTX were mixed in ethanol in a ratio of 20:0.5 and subsequently added dropwise to MQ containing phage particles at 65 °C. During synthesis, we interestingly observed a drastic difference in the color of the solution where plain liposomes and Φ_{NS} were used, despite keeping the concentration of MTX constant. The difference in the color of the solution of Φ_{NS} was supported by the increase in the intensity of MTX compared to plain lipos (Fig. 3A), given the same reaction conditions and concentration of MTX initially added.

We further explored if this difference was due to MTX or the presence of phage particles. For this, we repeated a similar procedure, wherein the plain lipos and Φ_{NS} were loaded with a

fluorescent dye, Nile red (NR). Surprisingly, a similar effect was again observed, where there was a significant difference in the color of the solution despite maintaining a constant concentration of NR initially loaded. This was supported by the increased intensity in the UV–Vis absorbance (Fig. 3B) and fluorescence intensity of NR (Fig. 3C) in the Φ_{NS} compared to the lipos. This effect was further validated with the encapsulation of another fluorescent dye, FITC, and a similar increase in the UV–Vis absorbance and fluorescence intensity (Fig. 3D and E) was observed in the Φ_{NS} compared to the control lipos. We also explored the role of lipids in this effect. However, when the same reaction was repeated using DPPC lipid, a similar effect was observed, thereby confirming the role of phage in enhancing the fluorescence of the encapsulated dye (Supplementary Fig. S3). For the first time, to the best of our knowledge, the role of phage in augmenting the optical properties of an encapsulated moiety is being explored.

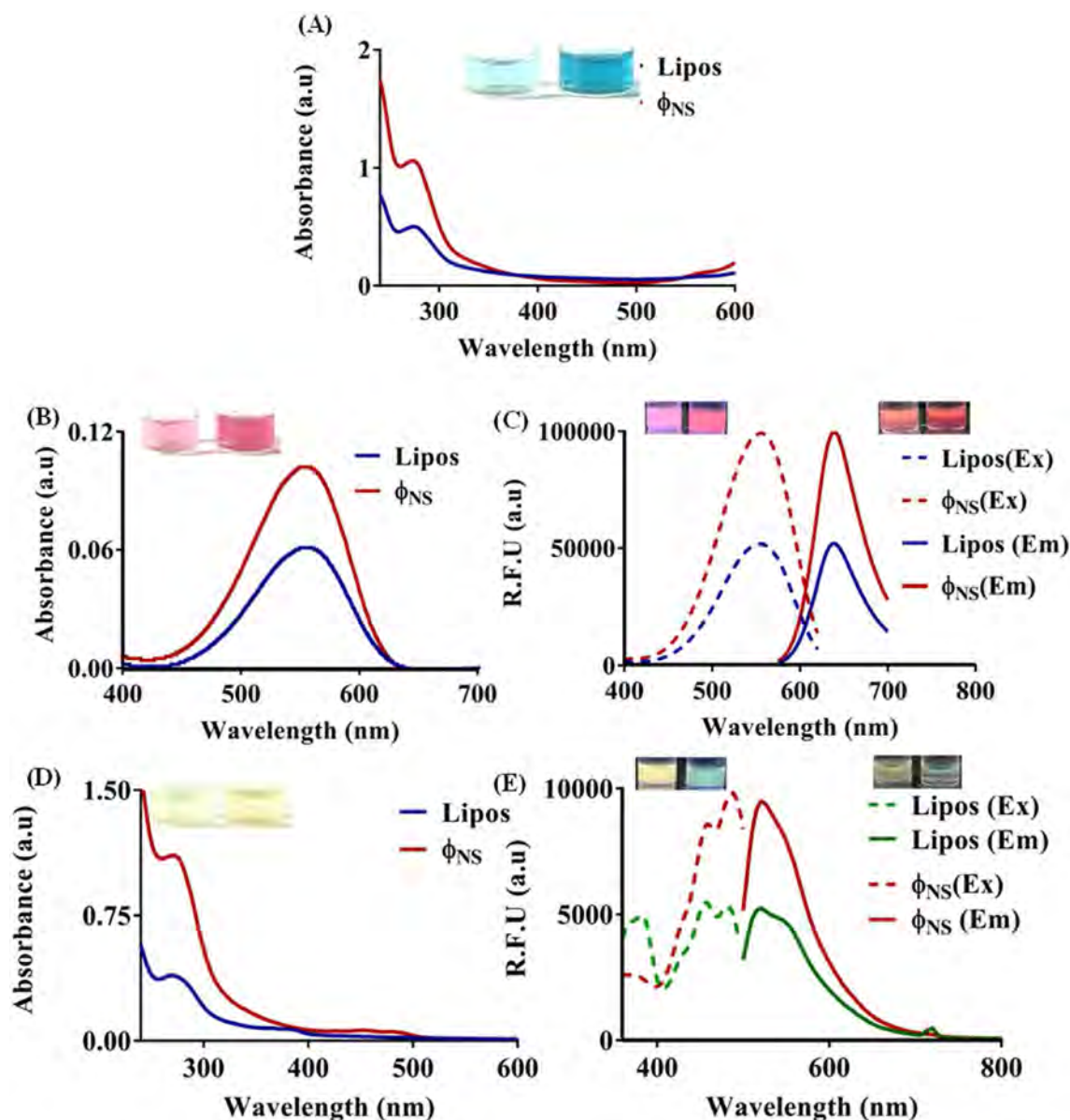


Fig. 3. Optical characterization of $\Phi_{NS}Au$ loaded with drug MTX and model dyes. (A) UV–Vis absorbance spectra of MTX loaded nanosomes (inset: photographs of the nanoparticles), (B) & (C) UV–Vis absorbance and fluorescence spectra of nile red loaded nanosomes respectively (Inset: Photographs of the nanoparticles under bright light and UV light), (D) & (E)) UV–Vis absorbance and fluorescence spectra of FITC loaded nanosomes respectively (Inset: Photographs of the nanoparticles under bright light and UV light).

3.4. Synthesis and characterization of $\Phi_{NS}AuM$

We further synthesized $\Phi_{NS}AuM$, wherein the Φ_{NS} loaded with MTX was coated with gold on its surface. UV–Vis absorbance

spectra revealed a broad spectrum in the range of 660–700 nm (Fig. 4A) showing its photothermal applicability. The average hydrodynamic diameter was observed to be 263 nm (Fig. 4B). However, the TEM imaging revealed a reduction in the size of the

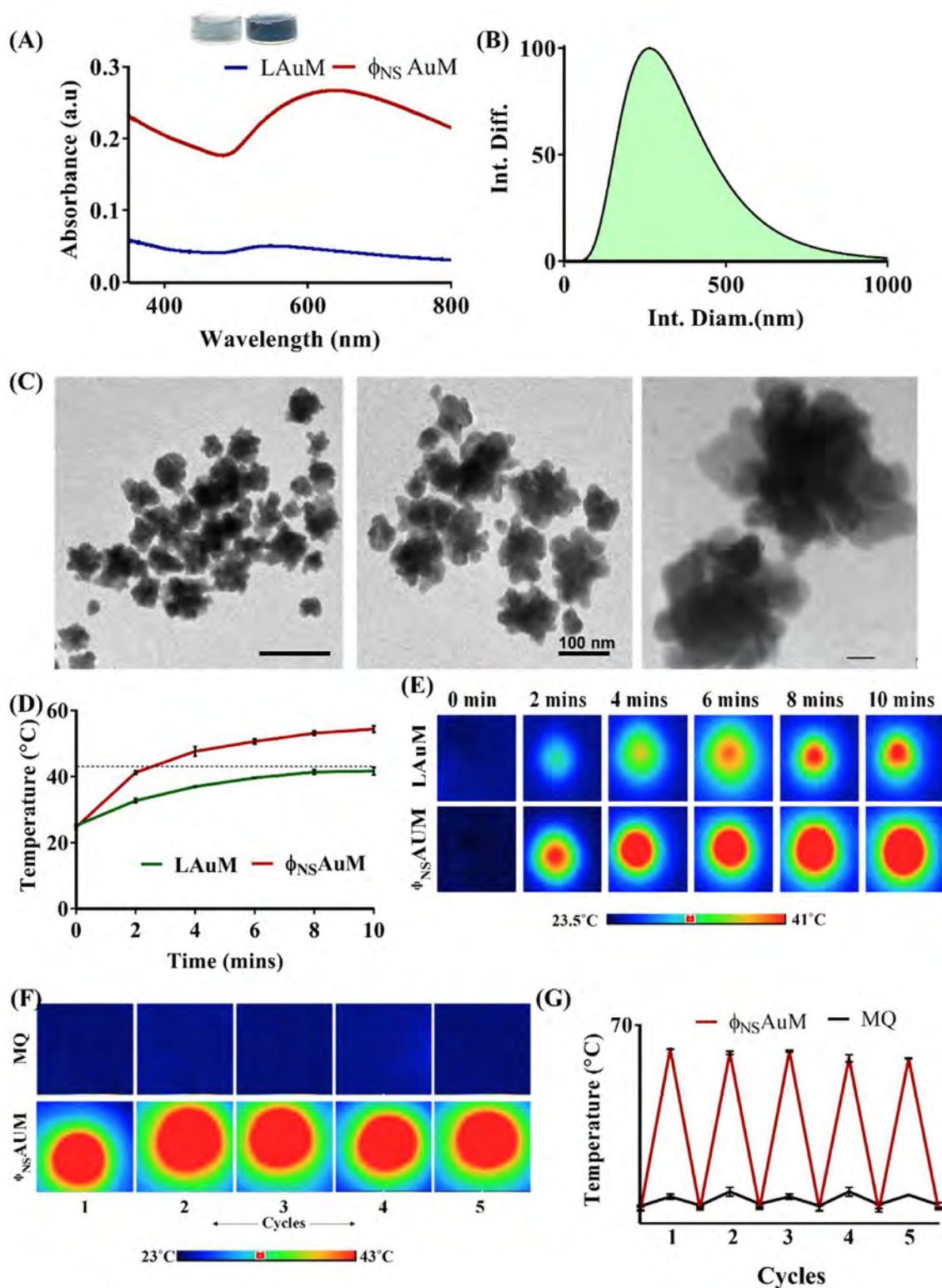


Fig. 4. Synthesis & Characterization of gold coated MTX loaded phage nanosomes. (A) UV–Vis absorbance spectra (Brightfield photographs of the synthesized nanoparticles), (B) Hydrodynamic diameter, (C) TEM images, (D) Temperature vs Time depicting the photothermal transduction efficacy of $\Phi_{NS}AuM$, (E) Thermal images (Scale bar in (C) represents 200 nm, 100 nm and 20 nm respectively). (F) & (G) Photothermal stability of $\Phi_{NS}AuM$ for 5 cycles of NIR irradiation.

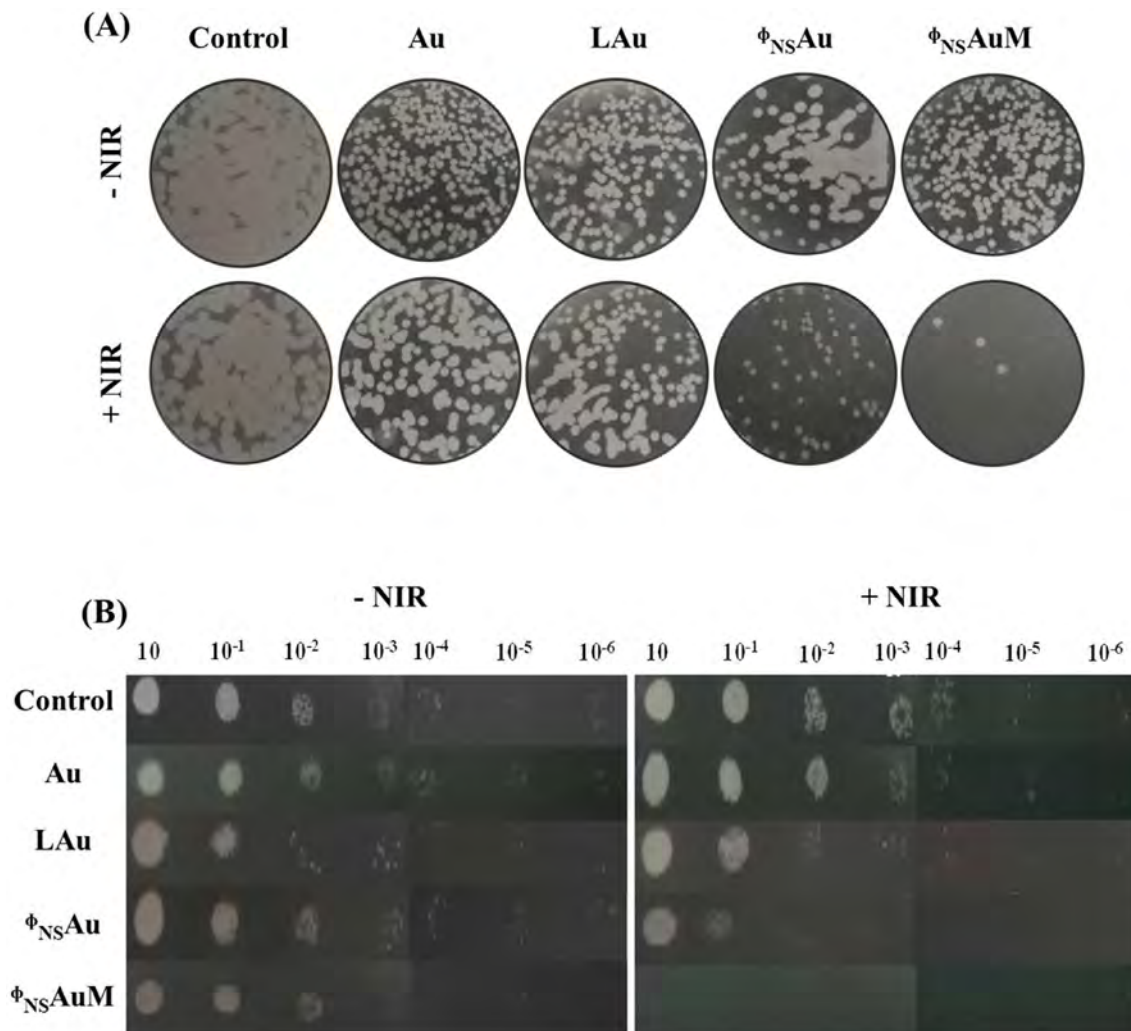


Fig. 5. Evaluation of anti-bacterial and anti-fungal activity of $\Phi_{NS}AuM$ mediated PTT. (A) Colony formation assay showing the effect of $\Phi_{NS}AuM$ mediated PTT on colony formation of *E. coli*, (B) Spot assay showing the antifungal effect of $\Phi_{NS}AuM$ mediated PTT against *C. albicans*.

nanoparticles in the range of 75–95 nm (Fig. 4C). The photothermal transduction efficacy of $\Phi_{NS}AuM$ was observed to be significantly higher than $\Phi_{NS}Au$, where the temperature rise upon 10 min of irradiation with a 690 nm laser was found to be $54.3 \pm 1^\circ\text{C}$ (Fig. 4D and E). The photothermal conversion efficiency of $\Phi_{NS}AuM$ was found to be 49.83% (Supplementary Fig. S15). Surprisingly, the presence of phage has also improved the photothermal transduction efficacy of the loaded nanosomes. This is evident from the low photothermal transduction efficacy of plain lipos loaded with MTX coated with gold. Hence, the use of a modified phage nanosome compared to a plain liposome as a template for photothermal tuning for gold nanoparticles was found to significantly improve the optical properties of the nanosomes. The photothermal stability of the synthesized $\Phi_{NS}AuM$ by irradiating of the samples repeatedly for five cycles. It was found that the temperature rise at the end of every cycle was, on average, 62.5°C (Fig. 4F and G). This photothermal stability was also supported by minimal/no difference in the UV–Vis absorbance spectrum (Supplementary Fig. S4A), and its hydrodynamic diameter (Supplementary Fig. S4B), which is concordant with the TEM image of $\Phi_{NS}AuM$ upon irradiation for 10 min (Supplementary Fig. S4C). Supplementary Fig. S5 and Table S2 summarize the hydrodynamic diameter of the synthesized nanosomes before and post-laser irradiation.

3.5. Anti-microbial activity

It is well-reported that cancer patients have a compromised immune system, which makes them prone to microbial infections. On the other hand, there are multiple instances where microbial infections have been a significant cause of cancer. Hence, a single nanopatform capable of synergistically and simultaneously killing both microbes and cancer cells is warranted. Thus, the anti-microbial potential of $\Phi_{NS}Au$ mediated PTT was evaluated in combination with MTX, previously reported to eradicate several bacterial and fungal infections.

3.5.1. Anti-bacterial activity

A colony formation assay was performed to understand the effect of $\Phi_{NS}Au$ and $\Phi_{NS}AuM$ mediated PTT on inhibiting the colony formation property of *E. coli*. 100 μL of the 8-fold serial dilution of treated *E. coli* inoculum was spread onto MH Agar plates with the appropriate controls. After 16 h of incubation at 37°C , a significant difference in the number of colonies formed was observed. As shown in Fig. 5A, it was observed that $\Phi_{NS}Au$ mediated PTT inhibited colony formation in *E. coli*. The effect $\Phi_{NS}Au$ was enhanced when combined with MTX ($\Phi_{NS}AuM$), which is evident from the fewer colonies formed when compared with controls.

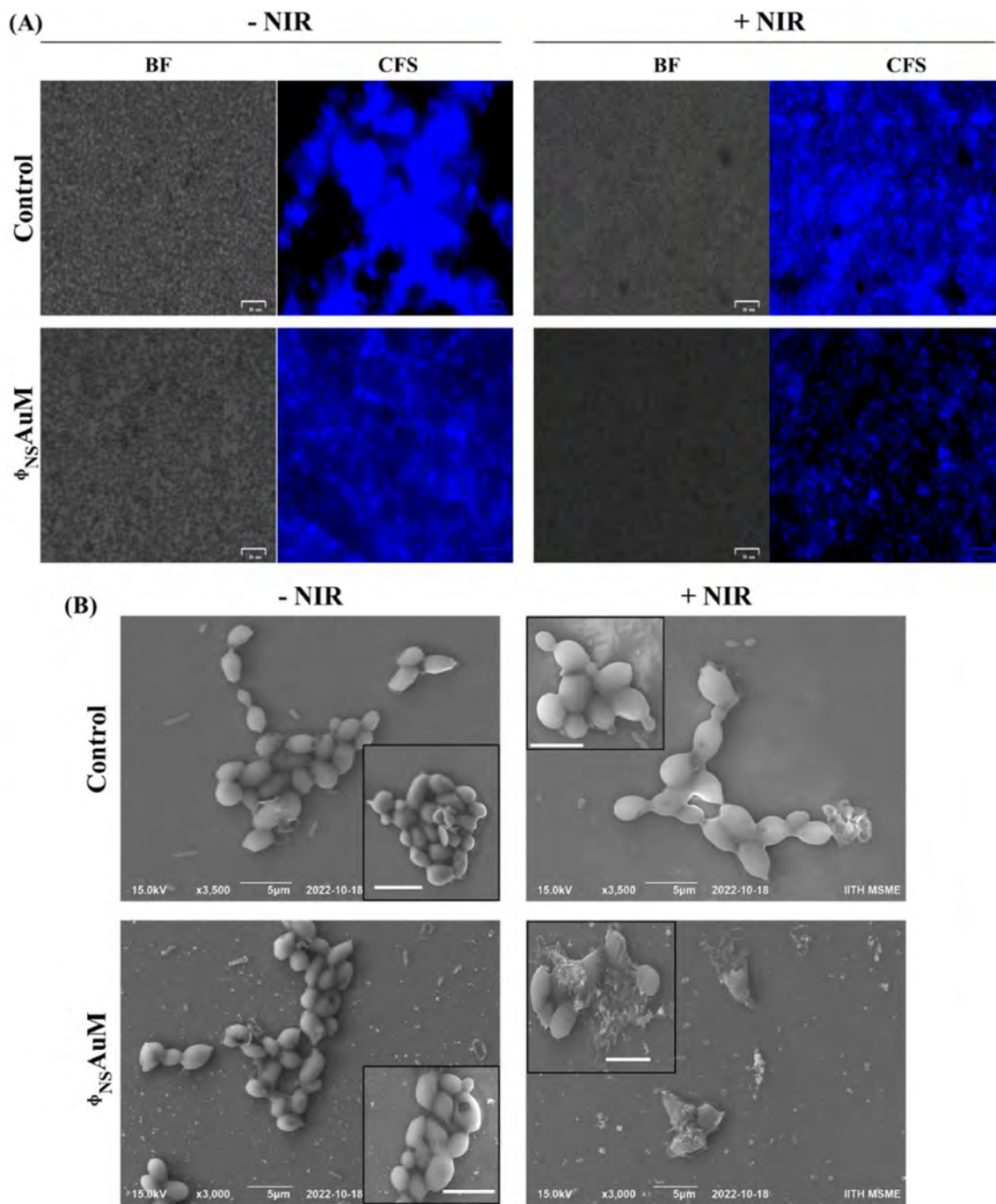


Fig. 6. Evaluation of morphological damage in *C. albicans* post $\Phi_{NS}AuM$ mediated PTT. (A) Calcofluor white stain (scale bar represents 100 μm) and, (B) FESEM analysis of *C. albicans* treated with $\Phi_{NS}AuM$ irradiated with 690 nm laser.

Thus, $\Phi_{NS}Au$ in combination with MTX could potentially be used as an anti-bacterial nanoformulation.

3.5.2. Anti-fungal activity

Spot assays were performed to elucidate the effect of $\Phi_{NS}Au$ mediated PTT in combination with MTX ($\Phi_{NS}AuM$) in preventing the colony formation of *C. albicans*. Briefly, 1 mL of 7-fold serial dilutions (10^{-1} , 10^{-2} , 10^{-3} , 10^{-4} , 10^{-5} and 10^{-6}) of treated *C. albicans* inoculum were spotted onto SD Agar plates with the appropriate controls. After 24 h of incubation at 37 $^{\circ}C$, the difference in the number of colonies and spot size at varying dilutions

was noticed. As shown in Fig. 5B, it was observed that $\Phi_{NS}Au$ mediated PTT in combination with MTX significantly reduced the fungal spores and prevented colony formation. Similarly, to understand the morphological defects in *C. albicans* post-treatment, the treated cultures were stained with equal volumes of Calcofluor white stain and 10% KOH. After 2–3 min, the cultures were observed under UV light in a live cell imager.

It was observed that the untreated control could form huge patches of colonies stained in blue (Fig. 6A), whereas in $\Phi_{NS}AuM$ treated group post-irradiation, there was a significantly lesser number of fungal cells; notably, no patches were observed. These

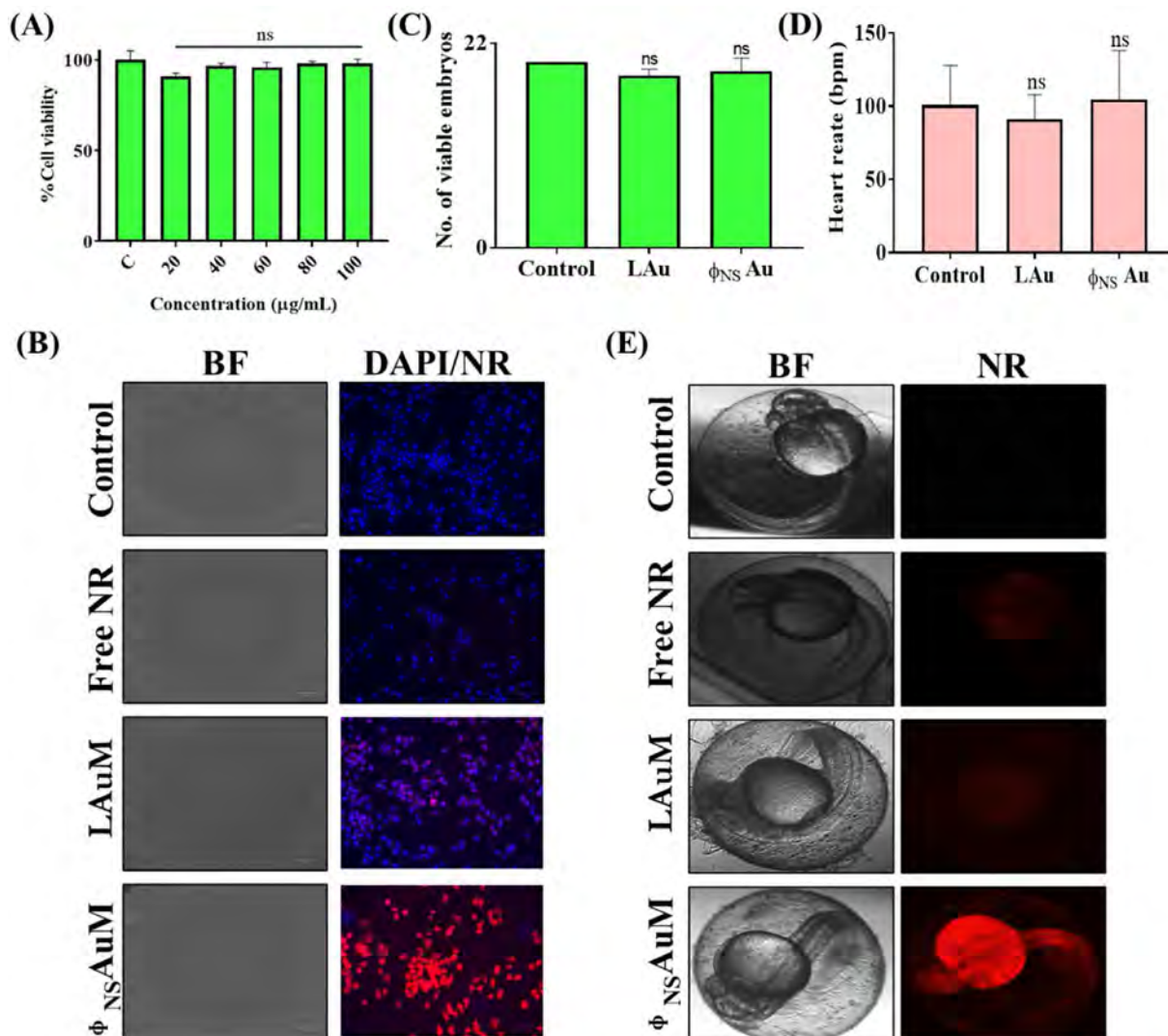


Fig. 7. Evaluation of biocompatibility & Internalization of $\Phi_{NS}AuM$ in cell lines & zebra fish embryo models. (A) Biocompatibility of $\Phi_{NS}Au$ in L929 cells, (B) Evaluation of internalization of $\Phi_{NS}Au$ in 4T1 cell lines (scale bar represents 100 μm) & (C) Survivability, (D) Evaluation of cardiotoxicity and (E) Internalization of $\Phi_{NS}Au$ in zebra fish embryos.

results were concordant with FESEM analysis, which revealed the morphological integrity of *C.albicans* in control groups. Whereas, in $\Phi_{NS}AuM$ treated group post-irradiation, a clear and distinct structural damage in the outer membrane further leading to the shrinkage of the cellular components was observed (Fig. 6B). This $\Phi_{NS}AuM$ prevents the growth of fungal mycelium and spore germination, thereby proving the effectiveness of a combinatorial synergistic effect of $\Phi_{NS}AuM$ in curbing the fungal growth and spread of infection.

3.6. In vitro & in ovo biocompatibility & internalization

Initially, the biocompatibility of $\Phi_{NS}Au$ was tested in L929 cells. The synthesized $\Phi_{NS}Au$ was observed to be compatible up to 100 $\mu g/mL$ with minimal/no toxicity observed upon 24 h of treatment, as shown in Fig. 7A. Further, the cellular internalization of $\Phi_{NS}Au$ was analyzed in 4T1 cells. Upon 5 h post-treatment, it was observed that there was a significant increase in internalization of $\Phi_{NS}Au$ when compared with LAu and free NR, which is evident from the bright red fluorescence in Fig. 7B. The mitochondrial localization of the $\Phi_{NS}Au$ nanosomes was evaluated using mitogreen staining and observed under fluorescence spectroscopy, wherein

the green fluorescence indicates mitochondrial staining and the red fluorescence indicates internalized $\Phi_{NS}Au$. The bright yellow fluorescence in the merged panel demonstrates the localization of the developed nanosomes within the mitochondria (Supplementary Fig. S12).

Fig. 7C depicts the survivability of the treated embryos, and it was observed that the developed $\Phi_{NS}Au$ did not cause any developmental defects or side effects compared with the control. The cardiac rhythm analysis was also performed on the treated embryos based on the dynamic pixel changes in a selected ROI of the embryonic heart region. The heart rate (bpm) was estimated and plotted in Fig. 7D and it is evident that the synthesized $\Phi_{NS}Au$ does not exhibit any side effects in the cardiac rhythm, thereby showing minimal/no cardiotoxicity.

We evaluated the uptake of free NR and NR-loaded LAu and $\Phi_{NS}Au$ in zebrafish embryos. Briefly, embryos at 1,2, and 3 dpf were treated with the nanosomes in 1X E3 media, and 24 h post-treatment, the uptake was analyzed using fluorescence microscopy. It is evident from Fig. 7E that the $\Phi_{NS}Au$ shows significantly enhanced uptake compared to free NR and LAu. Further, the embryos at 8 hpf were treated with $\Phi_{NS}Au$ and the survivability of the embryos was evaluated at 4 dpf.

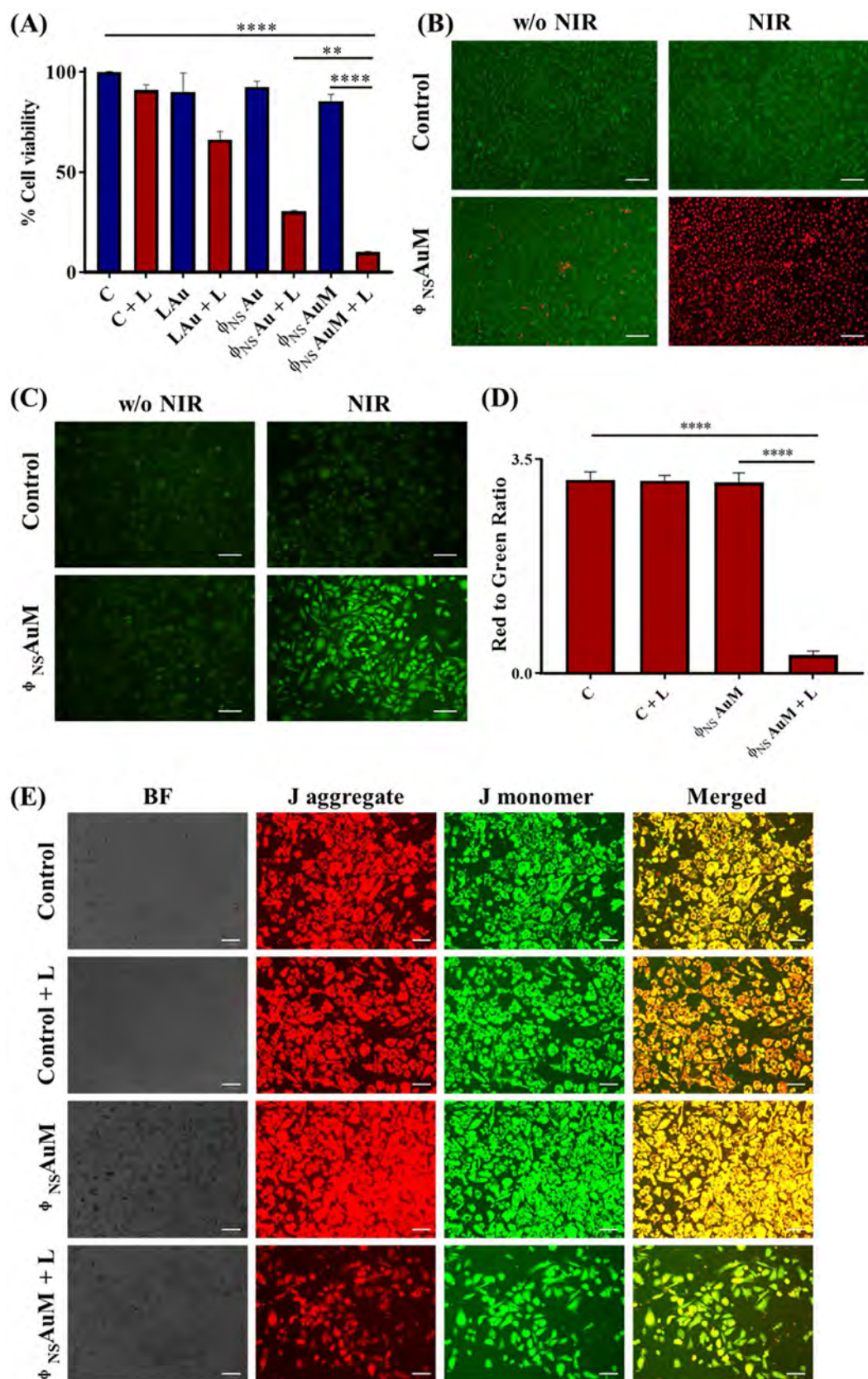


Fig. 8. Evaluation of in vitro anti-cancer efficacy. (A) Laser mediated cytotoxicity of $\phi_{NS}AuM$, (B) Representative Live/Dead staining using FDA/PI in 4T1 cells, (C) ROS generation in 4T1 cells treated with $\phi_{NS}AuM$ upon laser irradiation using DCFDA assay, (D&E) Evaluation of mitochondrial damage in 4T1 cells treated with $\phi_{NS}AuM$ upon laser irradiation using JC1 staining (D) Red to green fluorescence ratio depicting the mitochondrial damage and (E) Representative fluorescent images. (Scale bar in all the microscopic images represents 100 μm).

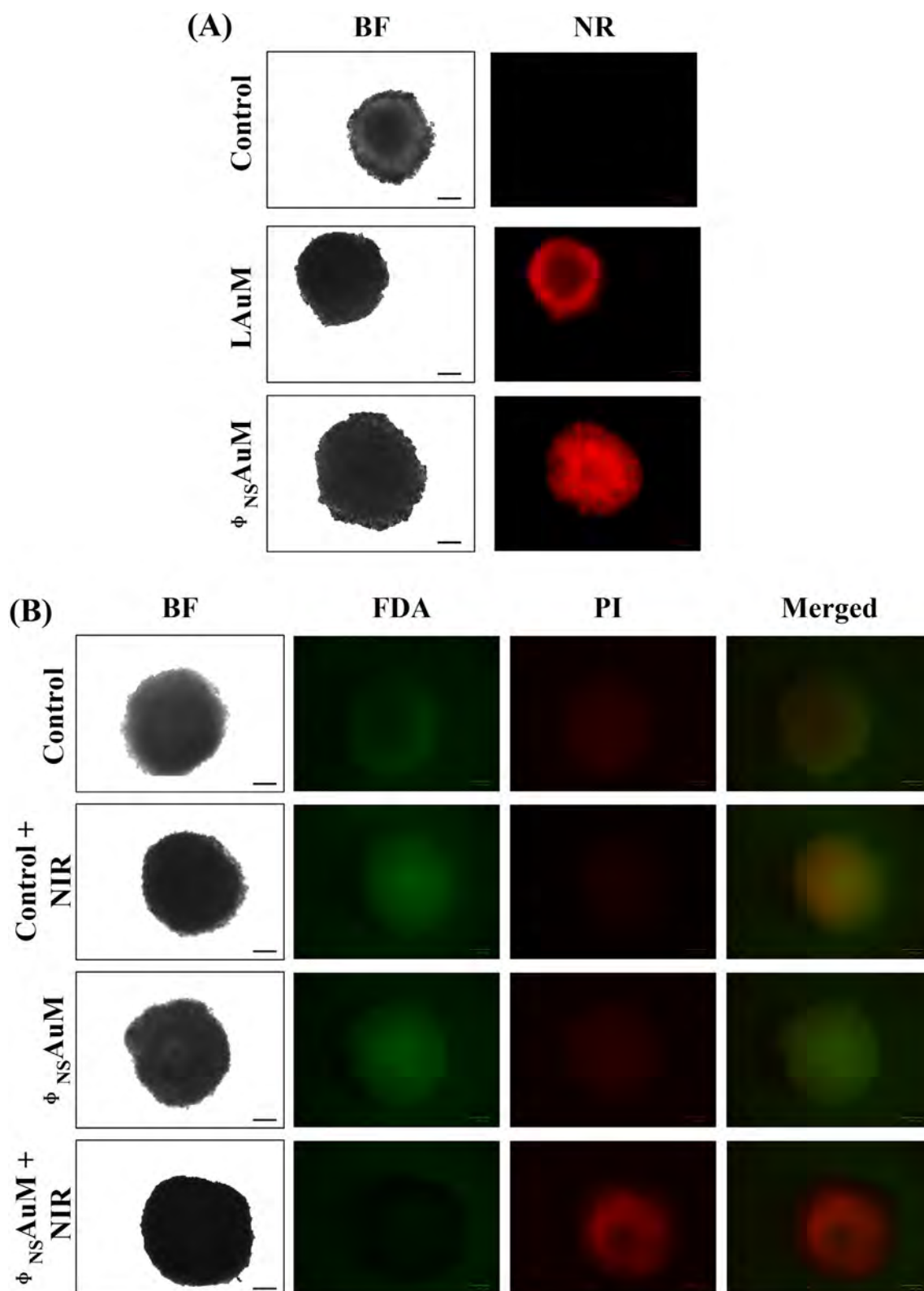


Fig. 9. Evaluation of uptake and PTT efficacy in 3D spheroids. (A) Evaluation of uptake of Nile Red loaded nanosomes in 3D spheroids of 4T1 cells. (B) Qualitative evaluation of photothermal efficacy of ϕ_{NSAuM} in 3D spheroids using live/dead staining (scale bar represents 100 μm).

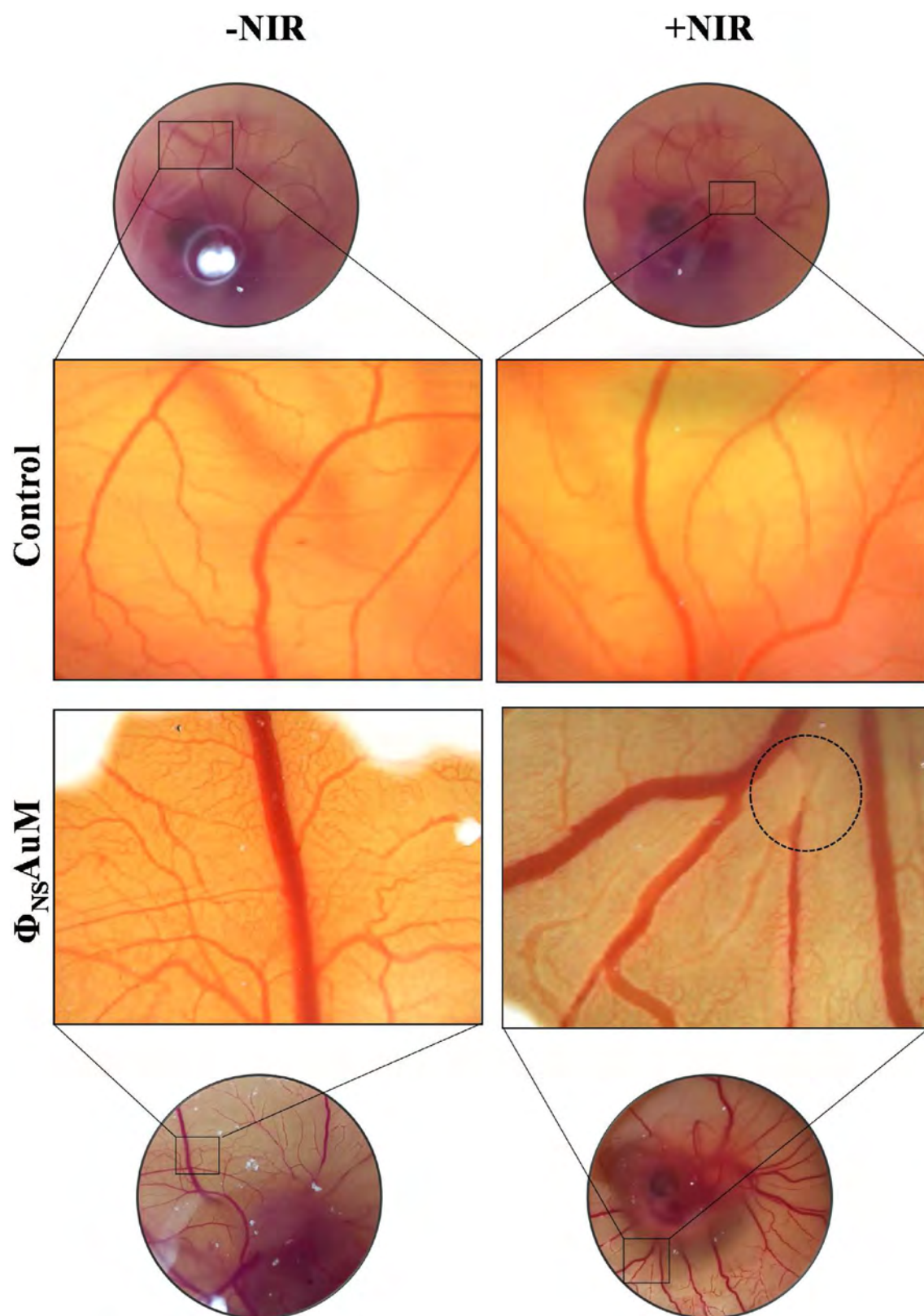


Fig. 10. Evaluation of neo-blood vessels rupturing properties of $\Phi_{NS}AuM$ mediated PTT using CAM assay in chick embryo model.

3.7. *In vitro* anti-cancer efficacy in 4T1 cell lines

The $\Phi_{NS}Au$ mediated PTT in combination with MTX was evaluated in 4T1 cells using the MTT assay. It was observed that, when compared with control and LAu, the percentage viability of cells treated with $\Phi_{NS}Au$ and $\Phi_{NS}AuM$ upon laser irradiation had significantly reduced, as shown in Fig. 8A. The effect was also qualitatively analyzed using the live/dead assay by adding FDA, staining the viable cells in green, and PI, staining the dead cells in red when imaged under a fluorescent microscope, as shown in Fig. 8B and Supplementary Fig. S7.

The oxidative stress induced by $\Phi_{NS}AuM$ mediated PTT was evaluated using the DCFDA assay. The cells were added with 10 μM DCFDA and were imaged under a fluorescent microscope upon laser irradiation. It was observed that the cells treated with $\Phi_{NS}AuM$ significantly generated a more significant amount of ROS compared to the control and LAu-treated groups, which is evident from the brighter and higher-intensity green fluorescence in $\Phi_{NS}Au$ and $\Phi_{NS}AuM$ treated groups, as shown in Fig. 8C and Supplementary Fig. S8.

Further, the effect of $\Phi_{NS}AuM$ -mediated PTT on the mitochondrial membrane potential was evaluated using JC1 staining. Upon encountering a healthy mitochondrial membrane, the JC1 dye forms an aggregate and fluoresces in red, whereas in the case of an unhealthy/dying mitochondrial membrane, the JC1 remains as a monomer and fluoresces in green. It is evident from Fig. 8E & Supplementary Fig. S9 that cells treated with $\Phi_{NS}AuM$ upon laser irradiation have caused significant mitochondrial damage due to enhanced ROS generation. The red-to-green fluorescence ratio was significantly lower for the cells treated with $\Phi_{NS}AuM$ + NIR laser compared with the control, as shown in Fig. 8D. Thus, the above studies reveal $\Phi_{NS}AuM$ as an excellent biodegradable PTT agent that could be potentially used for a synergistic anti-cancer application in combination with chemotherapeutic drugs.

3.8. *In vitro* anti-cancer efficacy in 4T1 spheroids

The uptake of LAuM and $\Phi_{NS}AuM$ was evaluated in 3D spheroids of 4T1 cells. Briefly, the spheroids were treated with Nile red loaded nanosomes, and upon 5 h post-treatment, the spheroids were imaged under the live cell imager (Zoe, BioRad, USA). It was observed that the $\Phi_{NS}AuM$ could internalize better into the core of the spheroids compared to the control LAuM as seen in Fig. 9A. Further, the photothermal efficacy was tested in the 3D spheroids. Briefly, the spheroids were treated with $\Phi_{NS}AuM$ and irradiated with a 690 nm laser for 10 min. The viability was then qualitatively tested by live/dead staining using FDA and PI 24 h post-treatment. As seen in Fig. 9B, the viability of the spheroid treated with $\Phi_{NS}AuM$ in combination with laser irradiation was reduced compared to the respective control groups, which is concordant with the results obtained in 2D cell lines. Thus, $\Phi_{NS}AuM$ could be utilized and explored as a potential photothermal agent.

3.9. *In ovo* CAM assay

The rupture of blood vessels upon $\Phi_{NS}AuM$ mediated PTT was evaluated using a CAM assay. It was observed that the chick embryos treated with $\Phi_{NS}AuM$, under laser irradiation displayed evident rupturing of blood vessels compared with their controls, as shown in Fig. 10 & Supplementary Fig. S10. This could also be due to the free radicals generated by PTT. Thus, $\Phi_{NS}AuM$ acts as a potential photothermal agent, having the ability to disrupt neo-blood vessels.

4. Conclusion

This study presents a unique bioinspired phage nanosome (Φ_{NS}) loaded with a known chemotherapeutic drug, MTX ($\Phi_{NS}M$), and further coated with gold ($\Phi_{NS}AuM$) to be tuned into NIR-absorbing PTT agents. The synthesized $\Phi_{NS}AuM$ displayed excellent photo-thermal transduction efficacy with significant stability. The NIR-mediated synergistic anti-bacterial efficacy of the $\Phi_{NS}AuM$ against *E. coli* was assessed using a colony formation assay. It was observed that $\Phi_{NS}AuM$, upon laser irradiation, could significantly eliminate *C. albicans*, as confirmed by spot assay, Calcofluor white staining, and FESEM analysis. When tested *in vitro* using 4T1 cell lines, the $\Phi_{NS}AuM$ caused considerable cell death upon laser irradiation (only ~10% viable cells) by enhanced cellular internalization, intracellular ROS, and mitochondrial damage. The rupturing of neo-blood vessels in a CAM model when treated with $\Phi_{NS}AuM$, upon laser irradiation demonstrated the blood vessel rupturing effect. Further, when tested *in ovo* using zebrafish embryos, the as said $\Phi_{NS}Au$ were found to be biocompatible with no cardiotoxicity and enhanced internalization compared with the control groups. Overall, the $\Phi_{NS}AuM$, a combination of living materials from phage and synthetic materials, serves as a single nanopatform for simultaneously eliminating microbial infections and tumor cells. However, *in vivo* research would be necessary to determine how these nanosomes may be used in the future.

Credit authorship contribution statement

Dokkari Nagalaxmi Yadav: conceptualization of the original idea, designing methodology, experiments, analysis of data, and writing the manuscript. **Sri Amruthaa Sankaranarayanan:** conceptualization of the original idea, designing methodology, experiments, analysis of data, writing manuscript. **Ajinkya Madhukar Thanekar:** Experiment. **Aravind Kumar Rengan:** conceptualization of the original idea, supervision, fund acquisition, discussion, and review.

Declaration of Competing Interest

The authors declare that they have no known competing financial interests or personal relationships that could have appeared to influence the work reported in this paper.

Data availability

Data will be made available on request.

Acknowledgment

The author would like to acknowledge MoE IMPRINT (4291), ICMR (No. 35/1/2020-GIA/Nano/BMS), ICMR-CoE grant, SUPRA (SPR/2022/000230), SERB-CRG (CRG/2020/005069), DBT NNT (BT/NNT/28/1386/2017), DST-AMT (DST/TDT/AMT/2017/227) and IITH/BME/SOCH3 project grants. The authors thank Dr. Manjula Reddy, Chief Scientist, CSIR-Centre for Cellular and Molecular Biology, Hyderabad, for providing the Bacteriophage Lambda (ATCC 23724-B2) and *E.coli* cultures. The author would like to acknowledge Krishna Chaitanya N (JRF) from Dr. Manjula Reddy's group, CCMB, for his continued support. The author would like to acknowledge Muriki Laxminarayana, Technical Superintendent, and Sukesh Kumar, a Ph.D. scholar from the MSME department, IIT Hyderabad, for SEM analysis. Author DNY would like to gratefully acknowledge DST-INSPIRE (DST/INSPIRE/03/2019/001517) for funding her fellowship. Author SAS would like to gratefully acknowledge MoE-PMRF (ID 2000832) for funding her fellowship. A fellowship from

the Council of Scientific and Industrial Research (CSIR) of the Government of India is gratefully acknowledged by the author, AMT. The authors would also like to acknowledge our labmates, Sunil Venkanna Pogu, Rupali Srivastava, Ananya Padmakumar, Tejaswani Appidi, Sajmina Khatun, and Himasree Buddhiraju, for their help and support. Graphical abstracts and schematics were created using the licensed version of [BioRender.com](#).

Appendix A. Supplementary data

Supplementary data to this article can be found online at <https://doi.org/10.1016/j.mtnano.2023.100348>.

References

- [1] P. Yadav, S.P. Singh, A.K. Rengan, A. Shanavas, R. Srivastava, Gold laced bio-macromolecules for theranostic application, *Int. J. Biol. Macromol.* 110 (2018) 39–53.
- [2] Y. Kanjanapan, D. Yip, Characteristics and risk factors for microbial infections during cancer immune checkpoint therapy, *Cancer Med.* 9 (2020) 9027–9035.
- [3] A. Zloza, Viruses, bacteria, and parasites – oh my! a resurgence of interest in microbial-based therapy for cancer, *J. Immunother. Cancer* 6 (2018) 4–6.
- [4] A. Hassan, J. Abdullah, K. Mohammed, A. Hasan, H.W. Al-kaim, Distribution of patients microbial infections with cancer disease of women, *Med. Leg. Update* (2021), <https://doi.org/10.37506/mlu.v2i12.2902>.
- [5] E. Reginato, Immune response after photodynamic therapy increases anti-cancer and anti-bacterial effects, *World J. Immunol.* 4 (2014) 1.
- [6] A. Belcheva, T. Irrazabal, A. Martin, Gut microbial metabolism and colon cancer: can manipulations of the microbiota be useful in the management of gastrointestinal health? *Bioessays* 37 (2015) 403–412.
- [7] Q. Georges, et al., Influence of neutropenia on mortality of critically ill cancer patients: results of a meta-analysis on individual data, *Crit. Care* 22 (2018) 326.
- [8] G.M. Haeusler, et al., Re-evaluating and recalibrating predictors of bacterial infection in children with cancer and febrile neutropenia, *EClinicalMedicine* 23 (2020), 100394.
- [9] S.S. Wang, et al., Clinical manifestations and prognostic factors in cancer patients with bacteremia due to extended-spectrum β -lactamase-producing *Escherichia coli* or *Klebsiella pneumoniae*, *J. Microbiol. Immunol. Infect.* 44 (2011) 282–288.
- [10] C.C. Chiou, A.H. Groll, T.J. Walsh, New drugs and novel targets for treatment of invasive fungal infections in patients with cancer, *Oncologist* 5 (2000) 120–135.
- [11] A. Dzutsev, et al., Microbes and cancer, *Annu. Rev. Immunol.* 35 (2017) 199–228.
- [12] M. Suganuma, T. Kuzuhara, K. Yamaguchi, H. Fujiki, Carcinogenic role of tumor necrosis factor- α inducing protein of *Helicobacter pylori* in human stomach, *J. Biochem. Mol. Biol.* 39 (2006) 1–8.
- [13] G.P. Bodey, et al., The epidemiology of *Candida glabrata* and *Candida albicans* fungemia in immunocompromised patients with cancer, *Am. J. Med.* 112 (2002) 380–385.
- [14] A.D. Alnuaimi, D. Wiesenfeld, N.M. O'Brien-Simpson, E.C. Reynolds, M.J. McCullough, Oral *Candida* colonization in oral cancer patients and its relationship with traditional risk factors of oral cancer: a matched case-control study, *Oral Oncol.* 51 (2015) 139–145.
- [15] A.K. Rengan, M. Jagtap, A. De, R. Banerjee, R. Srivastava, Multifunctional gold coated thermo-sensitive liposomes for multimodal imaging and photothermal therapy of breast cancer cells, *Nanoscale* 6 (2014) 916–923.
- [16] A.K. Rengan, et al., *In vivo* analysis of biodegradable liposome gold nanoparticles as efficient agents for photothermal therapy of cancer, *Nano Lett.* 15 (2015) 842–848.
- [17] S.P. Singh, et al., NIR triggered liposome gold nanoparticles entrapping curcumin as in situ adjuvant for photothermal treatment of skin cancer, *Int. J. Biol. Macromol.* 110 (2018) 375–382.
- [18] M. Liu, et al., An efficient antimicrobial depot for infectious site-targeted chemo-photothermal therapy, *J. Nanobiotechnol.* 16 (2018) 1–20.
- [19] W. Chen, et al., Bacteria-driven hypoxia targeting for combined biotherapy and photothermal therapy, *ACS Nano* 12 (2018) 5995–6005.
- [20] T. Appidi, et al., A plasmon-enhanced fluorescent gold coated novel lipopolymeric hybrid nanosystem: synthesis, characterization and application for imaging and photothermal therapy of breast cancer, *Nanoscale* 14 (2022) 9112–9123.
- [21] M.R. Oliva, S. Saini, Liver cancer imaging: role of CT, MRI, US and PET, *Cancer Imag.* 4 (2004) S42–S46.
- [22] D. Patel, et al., The cell labeling efficacy, cytotoxicity and relaxivity of copper-activated MRI/PET imaging contrast agents, *Biomaterials* 32 (2011) 1167–1176.
- [23] H. Yan, et al., Neoadjuvant nano-photothermal therapy used before operation effectively assists in surgery for breast cancer, *Nanoscale* 11 (2019) 706–716.
- [24] P. Gao, S. Sun, Y. Wang, Y. Wei, Y. Jiang, Biodegradable T2-phage-like Janus nanoparticles for actively-targeted and chemo-photothermal synergistic therapy, *Chem. Eng. J.* 428 (2022), 131284.
- [25] X.Y. Ma, B.D. Hill, T. Hoang, F. Wen, Virus-inspired strategies for cancer therapy, *Semin. Cancer Biol.* (2021), <https://doi.org/10.1016/j.semcancer.2021.06.021>.
- [26] Y.H. Chung, H. Cai, N.F. Steinmetz, Viral nanoparticles for drug delivery, imaging, immunotherapy, and theranostic applications, *Adv. Drug Deliv. Rev.* 156 (2020) 214–235.
- [27] G.F. Luo, W.H. Chen, X. Zeng, X.Z. Zhang, Cell primitive-based biomimetic functional materials for enhanced cancer therapy, *Chem. Soc. Rev.* 50 (2021) 945–985.
- [28] B. Cao, M. Yang, C. Mao, Phage as a genetically modifiable supra-macromolecule in chemistry, materials and medicine, *Acc. Chem. Res.* 49 (2016) 1111–1120.
- [29] K.S. Sunderland, M. Yang, C. Mao, Nanomedizin auf Phagenbasis: von Sonden zu Therapeutika für eine Präzisionsmedizin, *Angew. Chem.* 129 (2017) 1992–2022.
- [30] A. Catala, et al., Targeted intracellular delivery of trastuzumab using designer phage Lambda nanoparticles alters cellular programs in human breast cancer cells, *ACS Nano* 15 (2021) 11789–11805.
- [31] A. Shoaie-Hassani, et al., λ Phage nanobioparticle expressing apoptin efficiently suppress human breast carcinoma tumor growth in vivo, *PLoS One* 8 (2013) 2–13.
- [32] D.J. Müller, A. Engel, J.L. Carrascosa, M. Vélez, The bacteriophage ϕ 29 head-tail connector imaged at high resolution with the atomic force microscope in buffer solution, *EMBO J.* 16 (1997) 2547–2553.
- [33] T. Appidi, et al., Highly fluorescent polyethylene glycol-ascorbic acid complex for imaging and antimicrobial therapeutics, *Mater. Today Commun.* 29 (2021), 102987.
- [34] N. Revi, S.A. Sankaranarayanan, A.K. Rengan, A study on the role of eugenol encapsulated liposomes in facilitating neuron-microglia mediated wound recovery, *Materialia* 23 (2022), 101454.
- [35] A. Chinnasamy, Diagnostic yield of Calcofluor White in the identification of *Candida albicans* in oral squamous cell carcinoma, 2021, pp. 8–15.
- [36] R.S.K. Bhavasar, et al., Detection of *Candida* by calcofluor white, *Acta Cytol.* 54 (2010) 679–684.
- [37] Y. Zhang, et al., Near-infrared-triggered antibacterial and antifungal photodynamic therapy based on lanthanide-doped upconversion nanoparticles, *Nanoscale* 10 (2018) 15485–15495.
- [38] R. P.S. S.B. Alvi, N. Begum, B. Veeresh, A.K. Rengan, Self-assembled fluorosome-polydopamine complex for efficient tumor targeting and combined photodynamic/photothermal therapy of triple-negative breast cancer, *Biomacromolecules* 22 (2021) 3926–3940.
- [39] T. Appidi, et al., Light-triggered selective ROS-dependent autophagy by bioactive nanoliposomes for efficient cancer theranostics, *Nanoscale* 12 (2020) 2028–2039.
- [40] G. Yurtdaş-Kırımlıoğlu, K. Güleç, Ş. Görgülü, H.T. Kıyan, Oseltamivir phosphate loaded pegylated-Eudragit nanoparticles for lung cancer therapy: characterization, prolonged release, cytotoxicity profile, apoptosis pathways and in vivo anti-angiogenic effect by using CAM assay, *Microvasc. Res.* 139 (2022).